Klaver, Martijn, MacLennan, Scott A., Ibañez-Mejia, Mauricio, Tissot, François L.H., Vroon, Pieter Z. and Millet, Marc-Alban 2021. Reliability of detrital marine sediments as proxy for continental crust composition: the effects of hydrodynamic sorting on Ti and Zr isotope systematics. Geochimica et Cosmochimica Acta 310 , pp. 221-239. 10.1016/j.gca.2021.05.030

Publishers page: https://doi.org/10.1016/j.gca.2021.05.030

Reliability of detrital marine sediments as proxy for continental crust composition: the effects of hydrodynamic sorting on Ti and Zr isotope systematics

Martijn Klaver[1]*, Scott A. MacLennan[2], Mauricio Ibañez-Mejia[2], François L.H. Tissot[3], Pieter Z. Vroon[4] and Marc-Alban Millet[1]
[1]School of Earth and Environmental Sciences, Cardiff University, Park Place, Cardiff, CF10 3AT, United Kingdom
[2]Department of Geosciences, The University of Arizona, Tucson, AZ 85721, United States
[3]The Isotoparium, Division of Geological and Planetary Sciences, California Institute of Technology, Pasadena, CA 91125, United States
[4]Faculty of Science, Vrije Universiteit Amsterdam, De Boelelaan 1085, 1081HV Amsterdam, Netherlands
*corresponding author current address: Institut für Mineralogie, Westfälische Wilhelms-Universität Münster, Corrensstrasse 24, 48149 Münster, Germany; klaverm@uni-muenster.de

ABSTRACT

The isotopic composition of the detrital sediment record harbours a valuable proxy for estimating the composition of the erodible upper crust since the Archaean. Refractory elements such as titanium (Ti) and zirconium (Zr) can display systematic variations in their isotopic composition as a result of magmatic differentiation. Hence, for such elements, the isotope composition of detrital sediments could potentially be used to infer the average composition (e.g., SiO_2 content) of their source region, even when elemental systematics are obfuscated by weathering and diagenetic processes. A key premise of this approach is that the isotopic composition of sediments remains unbiased relative to their protolith. To what extent isotopic fractionation can occur during sedimentary processes, notably the hydrodynamic sorting of heavy mineral assemblages with contrasting isotopic compositions, remains poorly understood. We investigate the effects of such processes on the Ti and Zr isotope composition of a suite of detrital sediments from the Eastern Mediterranean Sea (EMS). These sediments are binary mixtures of two main provenance components, Saharan dust and Nile sediment, with strongly contrasting mineralogical and geochemical signatures.

The EMS sediments display clear evidence for hydrodynamic sorting of zircon, expressed as a large variation in Zr/Al_2O_3 and deviation of εHf relative to the terrestrial εNd-εHf array. Our new data, however, do not show pronounced Zr isotope variation resulting from either hydrodynamic sorting of zircon or sediment provenance. Although this agrees with theoretical models that predict negligible equilibrium zircon-melt Zr isotope fractionation, it contrasts with recent observations suggesting that kinetic Zr isotope fractionation might be a common feature in igneous rocks. For the EMS sediments, the negligible shift in Zr isotope composition through hydrodynamic sorting means that fine-grained samples accurately reflect the composition of their source. The nearly overlapping Zr isotope compositions of Sahara- and Nile-derived sediment, however, means that Zr isotopes, in this case, have insufficient resolution to be a useful provenance proxy.

Titanium behaves differently. A small but resolvable, systematic difference in Ti isotope composition is observed between the Sahara and Nile provenance components. Samples with a strong Saharan dust signature show some Ti isotope evidence for hydrodynamic sorting of oxides in tandem with zircon, but a much stronger effect is inferred for Nile sediment. Regression of the EMS sediment samples shows that the Ti isotope composition of the Nile-derived component is strongly fractionated compared to its protolith, the Ethiopian flood basalts. Whereas Ti in Nile sediment is carried in essentially unmodified concentration, and by inference isotope composition, from its sources to the delta, large-scale hydrodynamic sorting of Fe-Ti oxides occurs in the delta. This process decreases TiO_2/Al_2O_3 of the residual fine-grained sediment fraction and shifts its Ti isotope composition to heavier compositions. The potential of such an "oxide effect" in detrital sediments has implications for crustal evolution models that use Ti isotopes as a proxy for the proportion of felsic crust and can account for the observed scatter in the shale record.

KEYWORDS: detrital sediments; hydrodynamic sorting, Ti isotopes, Zr isotopes, Eastern Mediterranean Sea

1. Introduction

The sediment record holds valuable clues about the evolution of Earth's upper continental crust through time. Detrital sediments, such as shales, diamictites, and loess, are used as proxies for establishing compositional changes in the erodible crust since the Archaean (e.g., Taylor and McLennan, 1985; Condie, 1993; Gaschnig et al., 2016; Tang et al., 2016; Greber and Dauphas, 2019). Expanding on the traditional approach of using elemental ratios as proxies, a recent development is the use of the isotopic composition of "non-traditional" elements, for instance titanium (Ti), of Archaean to present-day detrital sediments as a tracer of the average crustal composition (Greber et al., 2017; Deng et al., 2019). This approach has two requirements: i) a contrast in the isotopic composition of mafic and felsic rocks, which results from mass-dependent isotopic fractionation during igneous differentiation; and ii) no bias (i.e., no isotopic fractionation) is introduced during weathering, transport, sedimentation, and diagenesis, which ensures that the isotopic composition of detrital marine sediments and sedimentary rocks accurately reflects that of their source.

Refractory, biologically inert elements with low solubilities in fluids, that also selectively partition into distinct phases during igneous differentiation can meet these criteria. We turn our attention to Ti and zirconium (Zr), two elements that are particularly promising for such studies. In the case of Ti, the first premise holds true as fractional crystallisation of isotopically light oxides drives the composition of the residual melt to isotopically heavier compositions (Millet et al., 2016; Greber et al., 2017; Johnson et al., 2019). The initial observation of a simple bijective relationship between SiO_2 content and Ti isotope composition (Millet et al., 2016; Greber et al., 2017) has, however, been revised in favour of a more nuanced understanding where notable variation in the Ti isotope composition of felsic rocks exists between tectonic settings and magma differentiation pathways (Deng et al., 2019; Aarons et al., 2020; Hoare et al., 2020). Likewise, mass-dependent Zr isotope variations are arguably controlled by the crystallization and removal of major and accessory phases in igneous systems and by the identity of those phases in a crystallizing magma, which have the potential to introduce marked Zr isotope differences between primitive and evolved igneous rocks (Ibañez-Mejia and Tissot, 2019; Inglis et al., 2019; Guo et al., 2020; Méheut et al., 2021).

Whether the second premise holds true for both systems and if the Ti and Zr isotope compositions of fine-grained marine sediments reflect that of their source, has not yet been demonstrated (Greber and Dauphas, 2019). A potential caveat is hydrodynamic sorting of dense minerals hosting these elements during sediment transport. This process is well-established for Zr as coarser sediments, such as turbidites, tend to have higher Zr/Al_2O_3 and unradiogenic Hf isotope compositions due to the concentration of dense zircon grains, and is commonly referred to as the "zircon effect" (e.g., Patchett et al., 1984; McLennan et al., 1990; Plank and Langmuir, 1998; Vervoort et al., 1999; Carpentier et al., 2009; Garçon et al., 2013). Clay-rich and other fine-grained sediments form the complementary zircon-depleted reservoir with lower Zr/Al_2O_3 and higher εHf. As zircon-enriched turbidites are a volumetrically minor component, the marine sediment record is on average zircon-depleted and characterised by high εHf for a given Nd isotope composition (Figure 1). The main phases that host Ti in igneous rocks, dense titanite and Fe-Ti oxides such as rutile, ilmenite, and titanomagnetite, are also resistant to physical and chemical weathering and form a common component of heavy mineral assemblages (e.g., Basu and Molinaroli, 1989; von Eynatten and Dunkl, 2012). As a result, Ti-rich phases have the potential to be concentrated in coarse sediment fractions along with zircon. The retention of isotopically fractionated Zr- and

Ti-rich accessory phases in these coarse fractions could hence bias the Ti and Zr isotope composition of the fine-grained detrital sediment record.

To investigate how reliable detrital sediments are in preserving the Ti and Zr isotope composition of their source, we have measured a suite of well-characterised marine sediments from the Eastern Mediterranean Sea (EMS) for their Ti and Zr isotope compositions. These samples are ideally suited for such a study as they document extensive hydrodynamic sorting effects (Klaver et al., 2015; see Figure 1). In addition, EMS sediments are heterogeneous mixtures of two distinct source components, felsic Saharan dust and mafic Nile sediment, which allows for explicit consideration of the influence of composition and mineralogy on the magnitude of isotopic fractionation resulting from sedimentary processes.

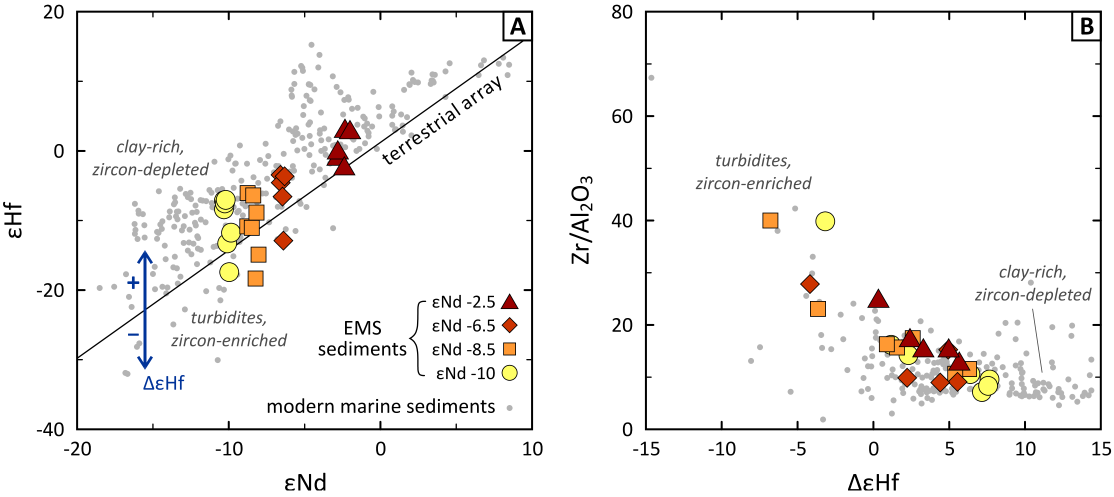

Figure 1. *The "zircon effect" resulting from hydrodynamic sorting of dense zircon into coarse, proximal deposits for global modern (<200 Ma) marine sediments (McLennan et al., 1990; Plank and Langmuir, 1998; Vervoort et al., 1999; Vlastélic et al., 2005; Prytulak et al., 2006; Van de Flierdt et al., 2007; Carpentier et al., 2008; Bayon et al., 2009; Carpentier et al., 2009; Vervoort et al., 2011) and the Eastern Mediterranean Sea (EMS) sediment samples measured for their Ti–Zr isotope composition in this study (Klaver et al., 2015). A) εNd versus εHf diagram calculated using CHUR values of 0.512630 and 0.282785 for* $^{143}Nd/^{144}Nd$ *and* $^{176}Hf/^{177}Hf$*, respectively (Bouvier et al., 2008). The ΔεHf parameter expresses the vertical deviation of a given sample from the terrestrial array of Vervoort et al. (2011), calculated as* $\Delta\varepsilon Hf = \varepsilon Hf - (1.55\varepsilon Nd + 1.21)$*; see blue arrow. B) ΔεHf versus* Zr/Al_2O_3 *(µg/g over wt.%).*

2. EMS sediments: provenance and the zircon-effect

To a first order, the detrital component of Neogene EMS sediments can be regarded as a binary mixture of aeolian dust transported from the northern Sahara region and sediment delivered to the EMS by the Nile river, the relative proportions of which are climate-driven and variable in space and time (e.g., Venkatarathnam and Ryan, 1971; Weldeab et al., 2002; Revel et al., 2010; Klaver et al., 2015). The two provenance components display a notable contrast in their mineralogy and geochemical composition (Figure 2). The sediment load of the Nile is very unevenly distributed between its main branches. Although the White Nile, which drains the Archaean Congo Craton, accounts for ca. 30 % of the annual discharge, its sediment load is nearly quantitatively lost in the Sudd marshes directly upstream of the confluence with the Blue Nile at Khartoum (Sudan). Consequently, more than 95 % of the suspended sediment load of the main Nile is derived from the Blue Nile and Atbara branches that have their source in the Cenozoic flood basalt province in the Ethiopian highlands (e.g., Foucault and Stanley, 1989; Padoan et al., 2011; Garzanti et al., 2015). As there are no other noteworthy tributaries to the Nile downstream of the Atbara confluence, Nile sediments preserve the "young and mafic" geochemical signature of relatively undifferentiated Ethiopian flood basalts that are the dominant lithology available for weathering. These primitive basalts are zircon-undersaturated and the small fraction of zircon that is present in heavy mineral assemblages in Nile sediment derives from the Proterozoic basement of the Nile in Sudan and Egypt (Garzanti et al., 2018). Zirconium in Nile sediments is predominantly hosted in volcanic lithics (the groundmass of the lavas) whereas ilmenite and titanomagnetite, but not titanite, are important carriers of Ti (Schneiderman, 1995; Garzanti et al., 2015).

In the Mediterranean Sea, Nile sediment is transported in a counter-clockwise gyre along the Levant margin before being progressively diluted towards the west by an aeolian dust component delivered by seasonal south-westerly winds (e.g., Goudie and Middleton, 2001; see Figure 2A). The main sources of dust transported towards the Mediterranean Sea are the Proterozoic Tuareg Shield in the Hoggar Massif (Algeria; e.g., Liégeois et al., 1994; Abdallah et al., 2007) and to a lesser extent the Western Sahara region. Dust derived from these sources is immature with a low chemical index of alteration (Moreno et al., 2006) and can be characterised as "old and felsic". The detrital component in the EMS sediment samples is diluted by up to 65 wt.% biogenic carbonate, which does not affect detrital trace element (including Ti and Zr) ratios and isotopic compositions (Klaver et al., 2015).

The sediment samples studied here for their Ti and Zr isotope composition were taken from Deep Sea Drilling Program (DSDP) and Ocean Drilling Program (ODP) cores in the EMS, complemented with box core samples from the African passive margin and Nile fan (Figure 2A). A detailed description and geochemical characterisation (major element, trace element and Sr-Nd-Hf-Pb isotope compositions) of the samples are provided by Klaver et al. (2015). The heterogeneous provenance of the EMS sediments is demonstrated by their range in εNd, which we use as a proxy for the relative proportion of Nile sediment (εNd = +2.6 ± 1.2) and Saharan dust (εNd = -13.8 ± 0.8) in the samples (Figure 2B). At a given εNd, the EMS sediments display significant variation in εHf as the result of the depletion or enrichment of dense zircon (Klaver et al., 2015). We have selected four groups of EMS sediment samples with similar εNd but variable εHf for this study (Figures 1 and 2B), which we will refer to as the εNd groups. The variation in εHf, conveniently expressed as ΔεHf – the deviation from the terrestrial array of Vervoort et al. (2011) – can be used as a proxy for the degree to which zircon is depleted or

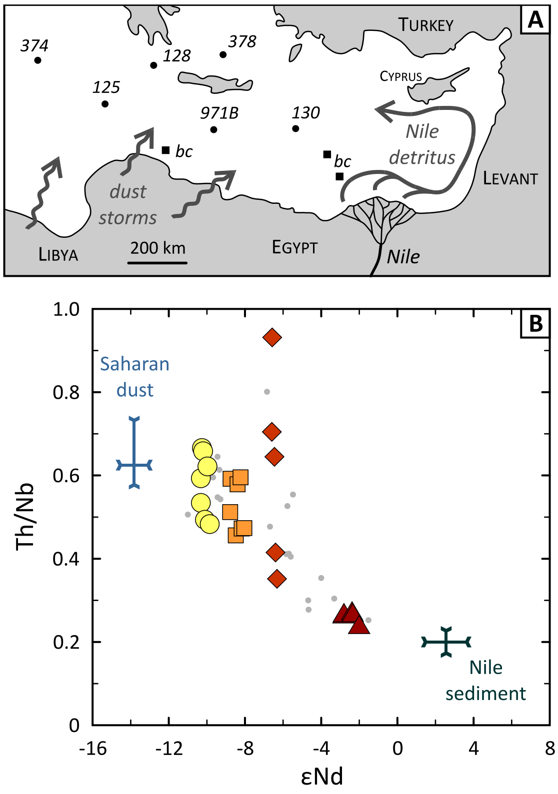

Figure 2. *A) Schematic map showing the two main sediment fluxes into the Eastern Mediterranean Sea (EMS), modified after Klaver et al. (2015). Detrital sediments delivered by the river Nile are transported in a counter-clockwise gyre along the Levant and diluted westward by a Saharan dust component. The EMS sediments in this study are derived from Deep Sea Drilling Program (DSDP; sites 125, 128, 130, 374 and 378) and Ocean Drilling Program (ODP; site 971B) drill cores, and box cores (squares labelled "bc") from the African passive margin and Nile fan. See Klaver et al. (2015) for a detailed description of the sites and samples; B) Geochemical characterisation of Eastern Mediterranean Sea sediments in relation to their two main provenance components; felsic Saharan dust and mafic Nile sediment (Klaver et al., 2015). Symbols for the εNd groups as in Figure 1. The excursion to higher Th/Nb for several samples from DSDP site 378 reflects a minor contribution from a high-Th/Nb component derived from the Neogene volcanic rocks from the Aegean region.*

enriched through hydrodynamic sorting. As shown in Figure 1, the EMS sediments display the expected negative correlation between ΔεHf and Zr/Al_2O_3 as the result of zircon accumulation in turbidites and samples from the African continental shelf. Samples with positive ΔεHf form the complementary, zircon-depleted reservoir consisting of more fine-grained detrital sediments. As will be discussed in detail in section 5.1., the EMS sediment samples display a general covariation between Zr/Al_2O_3 and TiO_2/Al_2O_3, suggesting that Ti-rich phases are concentrated in tandem with zircon.

3. Analytical techniques

Titanium isotope composition measurements were carried out at the Cardiff Earth Laboratory for Trace Element and Isotope Chemistry (CELTIC, Cardiff University) using the double spike protocol of Millet and Dauphas (2014). The sediment samples (10–20 mg aliquots) were digested in 1 mL 1:1 concentrated HF and HNO_3 at 140 °C for three days, after which 2 mL concentrated HNO_3 was added and the samples were evaporated to dryness at 90 °C. The digested samples were treated twice with concentrated HNO_3 and subsequently taken up in 5 mL 6 M HCl, to which 30–40 mg H_3BO_3 was added to ensure that any remaining fluorides were fully in solution. An aliquot of the dissolved sample, corresponding to ca. 5 µg Ti, was equilibrated with a ^{47}Ti–^{49}Ti double spike in a 52:48 proportion (Millet and Dauphas, 2014). Titanium was separated from the matrix using Eichrom DGA resin following a slightly modified version of the protocol pioneered by Zhang et al. (2011). The purified Ti fractions were treated repeatedly with concentrated HNO_3 and 30 % H_2O_2 to eliminate organic material.

Titanium isotope composition measurements were performed with a Nu plasma II multi-collector inductively-coupled plasma mass spectrometer (MC-ICP-MS) operated in medium resolution mode. Sample solutions with a concentration of 1.0–1.3 µg/mL Ti were introduced with an Aridus II desolvating nebuliser, which gave a total Ti ion beam intensity (sample plus double spike) of 40–60 V on amplifiers with 10^{11} Ω resistors in their feedback loop. The interference of Ca on ^{46}Ti and ^{48}Ti was monitored at mass 44 and corrected for if necessary (see supplementary Figure S1). A sample measurement consisted of 50 cycles of 10 s integration time. Each sample was bracketed by a measurement of the spiked OL-Ti reference material to allow a second-order correction of nonexponential instrumental mass fractionation. Data reduction was performed offline following the numerical double spike inversion approach of Rudge et al. (2009). Results are reported relative to the Origins Laboratory Ti reference material (OL-Ti) as $\delta^{49/47}Ti_{OL\text{-}Ti}$ (hereafter abbreviated to $\delta^{49/47}Ti$) according to the definition of Coplen (2011). Geological (BHVO-2, JB-2, and RGM-2) and Ti solution reference materials measured over the course of this study are in excellent agreement with published data and yield a pooled 2s intermediate precision of 0.022 ‰ (see supplementary Figure S2), which we take as the best estimate of the uncertainty of our measurements.

For Zr isotopes, ca. 150 mg aliquots of whole rock powder from each sample were fused with Li tetraborate flux in 1:2 proportion at 1000 °C for 10 min. The fusion cakes were subsequently digested in 3 M HNO_3 + 2 M HF and equilibrated with a ^{91}Zr–^{96}Zr double spike (Tompkins et al., 2020). Solutions were evaporated to dryness at 110 °C, taken up in 2 mL 3 M HNO_3 + 0.4 M H_3BO_3 to fully dissolve fluorides, and evaporated to dryness once more to remove residual F^- by the preferential production of volatile BF_3 gas. Zirconium purification followed a four-step ion-exchange procedure where Zr and Hf are first separated from major elements using Eichrom DGA resin. A "matrix clean-up" step was then performed using AG1-X8 resin to ensure complete removal of Fe and other major elements. Subsequently, Zr was separated from Hf using Eichrom Ln-spec resin, and from Mo and Ru, which are isobaric interferences on several Zr isotopes, using a final clean-up step with AG1-X8 resin. The Zr yield of this procedure is >90% and total procedural blanks including flux fusion are ca. 1 ng Zr, more than 3 orders of magnitude smaller than the amount of Zr processed for measurement and thus deemed negligible. More details on the ion-exchange purification procedure are provided in Ibañez-Mejia and Tissot (2019) and Tompkins et al. (2020).

Zirconium isotope measurements were carried out on a ThermoScientific Neptune Plus MC-ICP-MS at the Isotoparium (Caltech) using the methods from Tompkins et al. (2020). Measurements were made in static multi-collection, low-resolution mode using amplifiers equipped with amplifiers with 10^{11} Ω resistors in their feedback loop for all Zr isotopes and 10^{12} Ω resistors for monitoring isobaric interference of Mo at masses 95 and 98.

Sample solutions containing 82-92 ng/mL Zr were introduced with an Aridus 3 desolvating nebuliser using a nominal 100 µL/min PFA nebuliser (actual flow rate of 121 µL/min), which yielded a total Zr ion beam intensity (sample+double spike) of 38-45 V. A sample measurement consisted of 50 cycles of 4.2 s integration time, consuming 46 ng Zr per measurement including sample take-up, and was bracketed by a measurement of spiked NIST Zr reference material (see below). Each sample was measured two to five times during the session in a non-consecutive fashion. Data were processed offline employing a minimisation approach to solve the double spike equations obtained using all five measured Zr isotopes as described in detail in Tompkins et al. (2020). This contrasts with conventional inversion of the double spike equation, which uses three independent isotope ratios, and offers an internal check of the mass-dependency of the four ratios (see supplementary Table S1). We report the data as $\delta^{94/90}\text{Zr}_{\text{Zr NIST}}$ (hereafter abbreviated to $\delta^{94/90}$Zr), relative to a novel Zr reference material (provisionally named RM8299 Zr iRM) developed in collaboration with the United States National Institute of Standards and Technology (NIST) that, pending calibration, is referred to as Zr NIST.

Synthetic and natural Zr reference materials were measured over the course of this study to evaluate data quality. An aliquot of a SPEX Zr solution yielded $\delta^{94/90}$Zr = -0.324 ± 0.019 ‰ (2s, n = 37), which is in excellent agreement with the reference value (-0.325 ± 0.019 ‰) reported by Tompkins et al. (2020). Repeated measurements of geological reference materials (BHVO-2, BCR-2, RGM-2, and AGV-2; see supplementary Figure S3), which were interspersed with the EMS samples during the measurement session, are also in excellent agreement with previous studies. Literature data for Zr isotope compositions that are reported relative to IPGP-Zr and SRM 3169 are recalculated relative to Zr NIST when discussed in the text and shown in figures, using the following values: IPGP-Zr $\delta^{94/90}\text{Zr}_{\text{Zr NIST}}$ = -0.055 ± 0.002 ‰ (2se, n = 85) and SRM 3169 $\delta^{94/90}\text{Zr}_{\text{Zr NIST}}$ = 0.000 ± 0.007 ‰ (2se, n = 15).

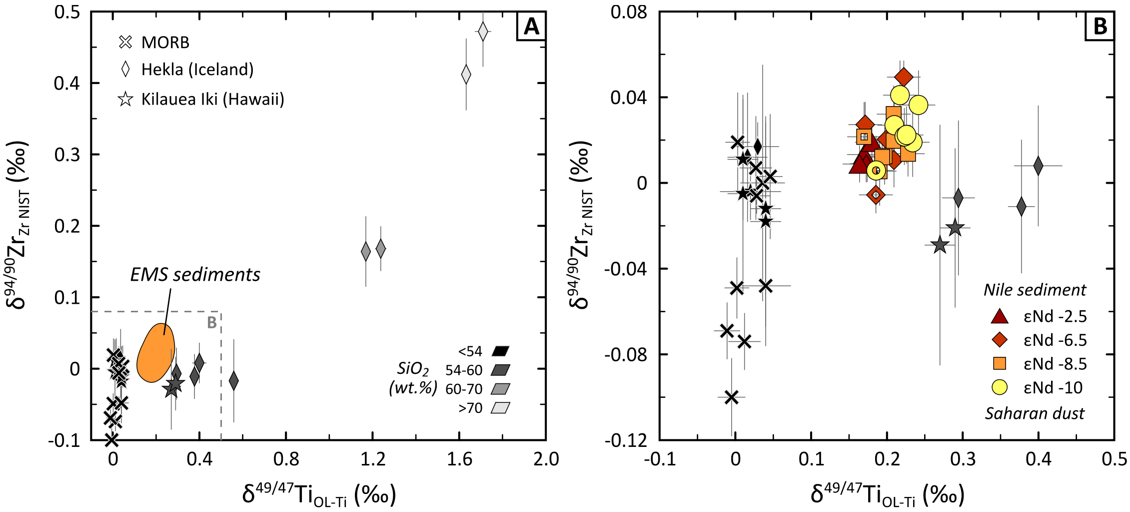

Figure 3. *The Ti–Zr isotope composition of the EMS sediments (open symbols for EMS sediments with ΔεHf <0) compared to mid-ocean ridge basalts (MORB) and igneous crystallisation suites from Hekla volcano (Iceland) and Kilauea Iki (Hawaii) that are colour-coded for SiO_2 content; data from Deng et al. (2018), Deng et al. (2019), Inglis et al. (2019) and Johnson et al. (2019).*

4. Results

The EMS sediment samples display a relatively narrow range in $\delta^{49/47}$Ti and $\delta^{94/90}$Zr from +0.164 to +0.242 ‰ and -0.006 to +0.050 ‰, respectively (Figure 3, Table 1). We use εNd as a proxy for provenance and have divided the EMS sediments into four groups based on their Nd isotope composition (Figure 2). Within these εNd groups, zircon-enriched samples with negative ΔεHf tend to have the lowest $\delta^{49/47}$Ti and $\delta^{94/90}$Zr although the differences are not statistically significant. The average compositions of the four εNd groups display a positive correlation between $\delta^{49/47}$Ti and $\delta^{94/90}$Zr, where the group with the highest εNd (-2.5) has on average (excluding samples with negative ΔεHf) the lowest $\delta^{49/47}$Ti (+0.172 ± 0.005; 2se, n = 5) and $\delta^{94/90}$Zr (+0.012 ± 0.009 ‰; 2se; n = 5; see

Table 2). Conversely, the group with the strongest Saharan dust signature (εNd = -10) has heavier Zr and Ti isotope compositions (+0.226 ± 0.009 ‰ and +0.028 ± 0.008 ‰, respectively; 2se, n = 6). Compared to igneous rocks for which both Zr and Ti isotope data are available, the EMS sediments show little variation (Figure 3). A suite of samples from Hekla volcano, Iceland, displays a marked increase in both $\delta^{49/47}$Ti (up to +1.7 ‰; Deng et al., 2019) and $\delta^{94/90}$Zr (up to +0.49 ‰; Inglis et al., 2019) with SiO_2 content (Figure 3) but the EMS sediments have Zr and Ti isotope compositions close to the mafic end of this differentiation trend.

5. Discussion

5.1. Isotopic variability in the EMS sediments through hydrodynamic sorting

5.1.1. Titanium isotopes

Hydrodynamic sorting of zircon is responsible for the range in ΔεHf observed in the EMS sediment samples (Klaver et al., 2015; see Figure 1). The positive correlation between tracers of zircon enrichment (ΔεHf, Al_2O_3/Zr) and Al_2O_3/TiO_2 within the Sahara dust-dominated sample groups (εNd = -10, -8.5 and -6.5) suggests that Ti does not behave as a purely detrital trace element (i.e., an element that is not fractionated during weathering, transport or deposition; see Plank and Langmuir, 1998) but that Ti is, at least to some extent, concentrated in tandem with zircon in coarse, proximal sediments (Figure 4A and B). The approximately factor of four to five decrease in Al_2O_3/Zr from zircon-depleted to zircon-enriched samples within these groups is, however, much more pronounced than the less than factor two variation observed in Al_2O_3/TiO_2, which is consistent with the higher Ti/Zr of clay-fraction minerals (Taylor and McLennan, 1985).

Provenance appears to exert a secondary control on Al_2O_3/TiO_2 of the EMS sediments. Samples in the group with the strongest Nile sediment signature (εNd = -2.5) have generally lower Al_2O_3/TiO_2 than the other EMS sediments while not showing notable zircon enrichment (ΔεHf between 0 and +6; Figure 4A). Lower Al_2O_3/TiO_2 in Nile sediment is in line with the high TiO_2 contents of the Ethiopian flood basalts (up to 5 wt.%; Pik et al., 1998; Kieffer et al., 2004) that are the dominant source of Nile sediment, compared to more felsic Saharan dust (Moreno et al., 2006; Castillo et al., 2008). Although it is difficult to fully disentangle the effects of provenance, it is clear that in particular sample groups with lowest εNd show evidence for hydrodynamic sorting of Ti-rich phases, but that this sorting effect is less pronounced than for zircon.

By virtue of their higher density compared to most silicate minerals, Fe-Ti oxides such as titanomagnetite ($Fe^{2+}_{1–2}[Fe^{3+},Ti]_{1–2}O_4$), ilmenite ($FeTiO_3$), and rutile ($TiO_2$), as well as the silicate mineral titanite ($CaTiSiO_5$), are the most plausible Ti-rich phases to be affected by hydrodynamic sorting. Due to the higher coordination number of Ti in Fe-Ti oxides than in silicate melts, Fe-Ti oxides are isotopically lighter (lower $\delta^{49/47}$Ti) than coexisting melt and silicate minerals (e.g., Millet et al., 2016; Johnson et al., 2019; Hoare et al., 2020; Wang et al., 2020). This dichotomy between isotopically light Ti hosted in dense Fe-Ti oxides and isotopically heavier Ti hosted in silicate (clay) minerals opens the possibility of Ti isotope fractionation during sediment transport and deposition. Hydrodynamic sorting of isotopically light oxides can produce Ti-enriched deposits with low $\delta^{49/47}$Ti while the complementary, Ti-depleted sediment fraction with higher $\delta^{49/47}$Ti can be transported further. The bias in $\delta^{49/47}$Ti of sediments imparted by this process is controlled by the Ti isotope composition, Ti content and proportion of the oxide phase that is retained (Figure 4D). At present, there are no constraints on the Ti isotope composition of titanite, which is also a common constituent of heavy mineral assemblages though it is not abundant in Nile sediments, and hence predicting the effects of hydrodynamic sorting of titanite is not yet possible.

The Ti isotope effects of hydrodynamic sorting of Fe-Ti oxides in our sample suite are small. Within the εNd groups, samples with the lowest Al_2O_3/TiO_2 and negative ΔεHf tend to have lower $\delta^{49/47}$Ti relative to other samples in that group (Figure 4C and D). As the range in Al_2O_3/TiO_2 is limited, the isotopic effect recorded in the EMS sediments is weak and introduces a barely resolvable variation of <0.03 ‰ on $\delta^{49/47}$Ti between samples within an εNd group. The mixing lines in Figure 4D indicate that the Fe-Ti oxides involved in hydrodynamic sorting have $\delta^{49/47}$Ti of 0.1–0.3 ‰ lower than the EMS sediment samples. This is broadly consistent with empirical constraints on $\Delta^{49/47}Ti_{oxide–melt}$ ranging from -0.2 to -0.6 ‰ (Millet et al., 2016; Johnson et al., 2019; Hoare et al., 2020).

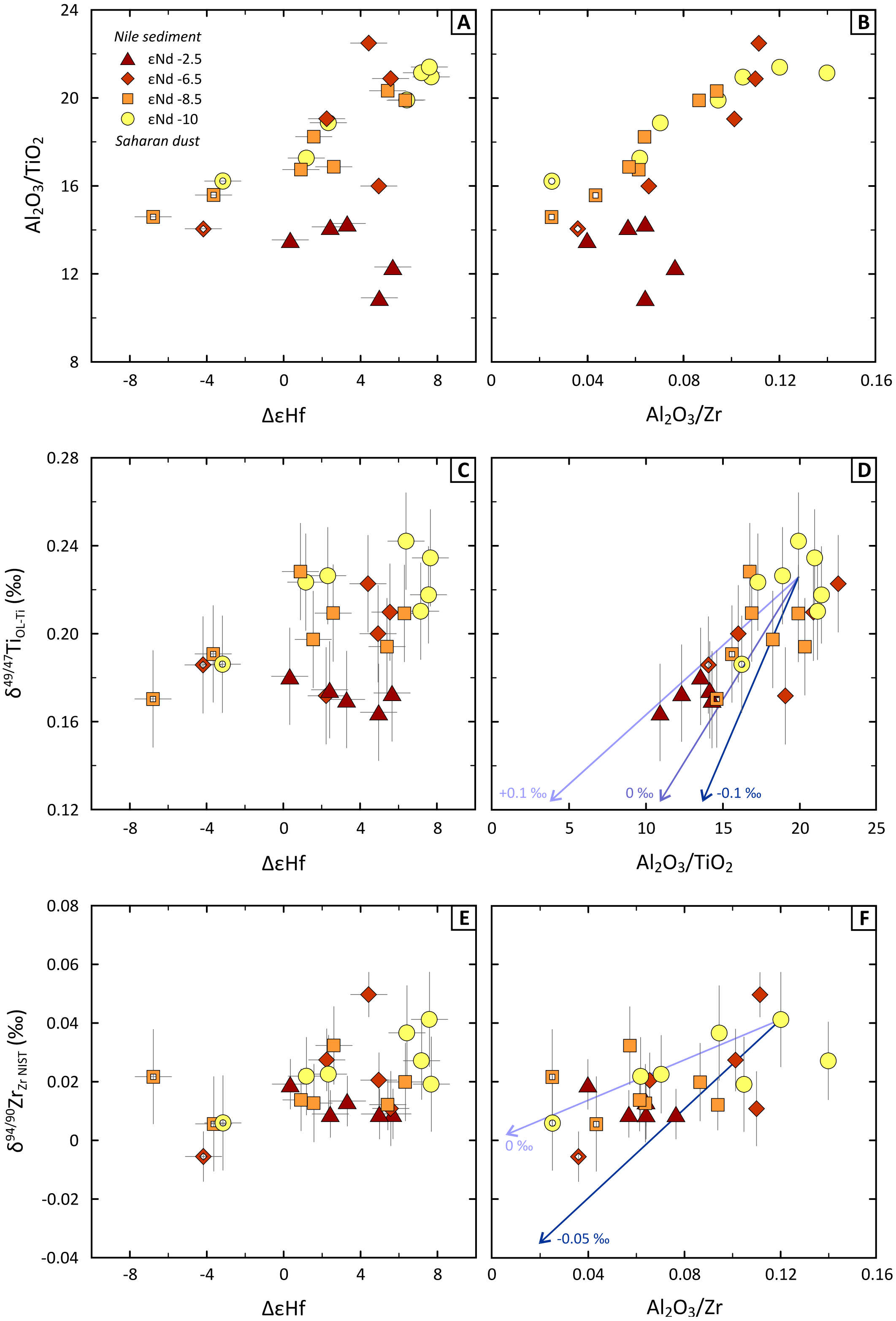

Figure 4. *The effects of hydrodynamic sorting in the EMS sediments. Open symbols for EMS sediments are samples with ΔεHf <0; uncertainties are smaller than symbol size when no error bars are shown. A) ΔεHf versus Al_2O_3/TiO_2; B) Al_2O_3/Zr (wt.% over µg/g) versus Al_2O_3/TiO_2; C) ΔεHf versus $\delta^{49/47}Ti$; D) Al_2O_3/TiO_2 versus $\delta^{49/47}Ti$; E) ΔεHf versus $\delta^{94/90}Zr$; F) Al_2O_3/Zr (wt.% over µg/g) versus $\delta^{94/90}Zr$. Panels (D) and (F) include model curves for enrichment in Fe-Ti oxides and zircon, respectively, through hydrodynamic sorting. These simple binary mixing lines assume that Fe-Ti oxides and zircon contain no Al_2O_3 and are plotted for different isotope compositions as noted in the labels. See caption for Figure 1 for a definition of ΔεHf.*

5.1.2. Zirconium isotopes

The Zr isotope effect of zircon accumulation and depletion in the EMS sediments is surprisingly small and $\delta^{94/90}$Zr shows hardly any systematic variation with ΔεHf and Al_2O_3/Zr (Figure 4E and F). Some samples with a clear zircon accumulation signature (negative ΔεHf, low Al_2O_3/Zr) have marginally lower $\delta^{94/90}$Zr but mass balance constrains the Zr isotope composition of accumulated zircon to be only marginally lighter than the clay minerals that host the remaining Zr. There is significant debate about the sign and magnitude of Zr isotope fractionation between zircon and silicate melt. Based on the systematic variation in $\delta^{94/90}$Zr of a suite of lavas from Hekla volcano (Iceland), which were assumed to be linked exclusively through fractional crystallisation (Figure 3), Inglis et al. (2019) deduced a value of ca. -0.5 ‰ for $\Delta^{94/90}\mathrm{Zr}_{\mathrm{zircon–melt}}$. A subsequent laser-ablation ICP-MS study of zircon in mafic to intermediate plutonic rocks from the Gangdese arc seemed to corroborate this result (Guo et al., 2020) as those authors argued that Zr isotope zoning in zircon could be explained by fractional crystallisation at $\Delta^{94/90}\mathrm{Zr}_{\mathrm{zircon–melt}}$ between -0.1 and -0.5 ‰. Conversely, Ibañez-Mejia and Tissot (2019) concluded that the large variation in $\delta^{94/90}$Zr of zircon (ca. 5 ‰) and baddeleyite (ca. 2.5 ‰) in residual melt pockets of an anorthositic cumulate from the Duluth Complex required a notably positive $\Delta^{94/90}\mathrm{Zr}_{\mathrm{zircon–melt}}$ of ca. +1 ‰.

The disparate observations from natural samples might be explained by theoretical studies that propose that equilibrium Zr isotope fractionation between common Zr-rich accessory minerals (zircon and baddeleyite) and melt is negligible at magmatic temperatures and that the observed $\delta^{94/90}$Zr heterogeneity is driven by kinetic fractionation (Chen et al., 2020; Méheut et al., 2021). These *ab initio* calculations employ different Zr-bearing silicate minerals where Zr is hosted in VI-fold coordination (vlasovite, Ca-catapleiite) as proxies for the Zr bonding environment in silicate melts. Despite this caveat, the two studies yield comparable estimates of $\Delta^{94/90}\mathrm{Zr}_{\mathrm{zircon–melt}}$ in the order of -0.08 to -0.02 ‰ at 700–1000 °C, from which they conclude that the large isotopic variability in natural zircon has to be caused by kinetic fractionation in diffusive boundary layers in the melt adjacent to growing crystals (Chen et al., 2020; Méheut et al., 2021). The Zr isotope homogeneity of zircon megacrysts that are commonly used as reference materials (Mud Tank, 91500) lends additional support for negligible equilibrium zircon-melt Zr isotope fractionation (Zhang et al., 2019; Tompkins et al., 2020).

A lack of pronounced variation in $\delta^{94/90}$Zr over the wide ranges in Al_2O_3/Zr or ΔεHf in the groups with εNd of -10, -8.5, and -6.5 seems to preclude either a distinctly positive or negative value for $\Delta^{94/90}\mathrm{Zr}_{\mathrm{zircon–melt}}$ in the Saharan dust protolith. By inference, the isotopic composition of zircon involved in hydrodynamic sorting can only be, on average, marginally lighter than bulk sediment samples (Figure 4F). Subsolidus re-equilibration is unlikely to homogenise kinetic fractionation effects in the Saharan dust protolith, notably the predominantly Proterozoic granitoids of the Tuareg Shield, because diffusion of Zr^{4+} in zircon is far too slow to cause a detectable change in $\delta^{94/94}$Zr (Tompkins et al., 2020). Rather, equilibrium zircon crystallisation at a $\Delta^{94/90}\mathrm{Zr}_{\mathrm{zircon–melt}}$ close to zero might have been sufficiently slow to inhibit significant kinetic fractionation of Zr in the melt during zircon growth. This shows that kinetic Zr isotope fractionation and large inter-mineral variation in $\delta^{94/90}$Zr may not always be a natural consequence of igneous zircon crystallisation.

An alternative, but arguably somewhat *ad hoc* interpretation, is that the Zr isotope consequences of hydrodynamic sorting of zircon might be self-cancelling. If the petrologic history of zircon nucleation and associated kinetic isotope fractionation in crystallizing melts is indeed behind the markedly positive and negative $\delta^{94/90}$Zr in natural zircon (Chen et al., 2020; Méheut et al., 2021) rather than being driven by a more systematic equilibrium fractionation mechanism, then it is possible that hydrodynamic sorting of isotopically light and heavy zircon in zircon-rich detrital sediments might result in a negligible net effect at the bulk sediment scale. Although it is not possible to evaluate this hypothesis using our EMS sample set as no heavy mineral separates are available, it can be tested in the future by determining the Zr isotope composition of detrital zircon and their host bulk rocks in clastic sedimentary environments.

In summary, hydrodynamic sorting of zircon and possibly baddeleyite does not introduce a large bias in $\delta^{94/94}$Zr between EMS sediment samples within an εNd group. It remains unclear why the EMS sediments should lack significant Zr isotope heterogeneity imparted by hydrodynamic sorting of zircon despite the clear evidence for this process from trace element and Nd-Hf isotope systematics.

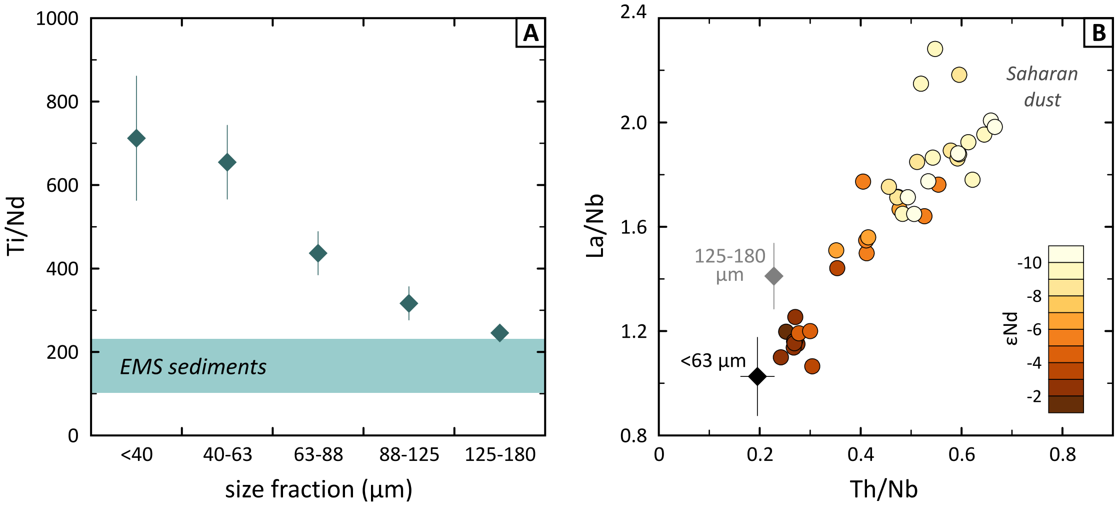

***Figure 5.** The Ti–Zr isotope composition of Nile sediment and Saharan dust derived from regression of the EMS sediment data. A) εNd versus Ti/Nd; B) εNd versus $\delta^{49/47}$Ti; C) εNd versus Zr/Nd; D) εNd versus $\delta^{94/90}$Zr. Dark green stars are individual Nile sediment samples (Garzanti et al., 2015); the average composition of Saharan dust and Nile sediment is shown by the crosses or grey bars (2s uncertainty for Ti/Nd and Zr/Nd, 2se for εNd; see Table 2). Open symbols for EMS sediments are samples with ΔεHf <0 and/or elevated Zr/Nd; these samples experienced zircon accumulation and are thus excluded from the average composition of the EMS sediment groups that were used in the regressions. The blue shaded fields are the 95 % confidence envelopes of the regressions; see main text and supplementary material for details.*

5.2. Ti-Zr isotopes in the sedimentary system

From trace element and radiogenic isotope systematics, it is well established that EMS sediments are binary mixtures of Saharan dust and Nile sediments (e.g., Venkatarathnam and Ryan, 1971; Weldeab et al., 2002; Revel et al., 2010; Klaver et al., 2015). This framework can be used to constrain the Ti–Zr isotope composition of these two source components and investigate the potential of isotopic fractionation during weathering and transport to the EMS. We use εNd as a reliable proxy for the relative proportions of Nile sediment and Saharan dust in the EMS sediment samples and as the basis for regressions versus Ti/Nd, $\delta^{49/47}$Ti, Zr/Nd and $\delta^{94/90}$Zr (Figure 5).

We compiled εNd and trace element data for the two provenance components from the literature (see Table 2 and supplementary Dataset 1). For Saharan dust, no combined Nd isotope and trace element datasets are available and hence only the average composition can be shown in Figure 5. Trace element data for Saharan dust were derived from direct analyses of soils and dust in the Hoggar Massif and Western Sahara (Moreno et al., 2006; Castillo et al., 2008) and aerosols collected in the Mediterranean region during dust storms (Moreno et al., 2010). The Nd isotope composition of Saharan dust was estimated from <30 µm soil samples in the northern Sahara region combined with aerosols collected during dust storms (Grousset et al., 1988; Grousset et al., 1990; Grousset et al., 1992; Henry et al., 1994; Grousset et al., 1998; Grousset and Biscaye, 2005; Revel et al., 2010).

The composition of the Nile-derived component in the EMS sediments is estimated from overbank clay/silt deposits (<63 µm fraction), which represent the fine-grained suspended load of the Blue Nile, Atbara river and Main Nile (Revel et al., 2010; Padoan et al., 2011; Garzanti et al., 2015). For some Nile sediment samples, both trace element and εNd data are available and these are shown individually in Figure 5, but the average compositions shown in Figure 5 incorporate all available data. Suspended Nile sediments show systematic variation in Ti/Nd as a function of grain size, with coarser fractions having lower Ti/Nd than the finer fractions (Figure 6). In other river systems, basaltic erosion products are commonly overrepresented in finer sediment fractions relative to coarser fractions (Garçon and Chauvel, 2014; Bayon et al., 2015). This also appears to be the case for the Nile where high-Ti/Nd detritus of the Ethiopian flood basalt province is the dominant component (>95 %) in the silt-sized (<63 µm) suspended sediment fractions (Garzanti et al., 2015). Titanium is hosted in detrital titanomagnetite and ilmenite grains that are predominantly present in these finest fractions of suspended Nile sediment. Coarser suspended sediment fractions and bed load are diluted by quartz, feldspar and amphibole, which are at least partly derived from erosion of the crystalline basement in the course of the Nile, causing a decrease in Ti/Nd. In any case, silt-sized Nile sediments have the highest potential to be transported past the delta and further out into the EMS relative to sand-sized fractions. Grain size data for EMS sediments support this assertion as typical median grain sizes are <10 µm with <15 % coarser than 32 µm (Bartolini et al., 1975; Revel et al., 2010). Furthermore, <63 µm suspended Nile sediment is an excellent match to the Nile-derived component in the EMS sediments in terms of trace element ratios that are sensitive to sediment provenance, such as Th/Nb, La/Nb, and Rb/Nb and εNd (Klaver et al., 2015; see Figure 6), and hence we use this as the best estimate of the Nile-derived component.

The shape of binary mixing lines in εNd versus $\delta^{49/47}$Ti or $\delta^{94/90}$Zr space is determined by Ti/Nd and Zr/Nd of the two mixing components, respectively. Hence, we first investigate whether the EMS sediment samples fall on a mixing line between Saharan dust and Nile sediment in εNd versus Ti/Nd and Zr/Nd space (Figure 5A and C).

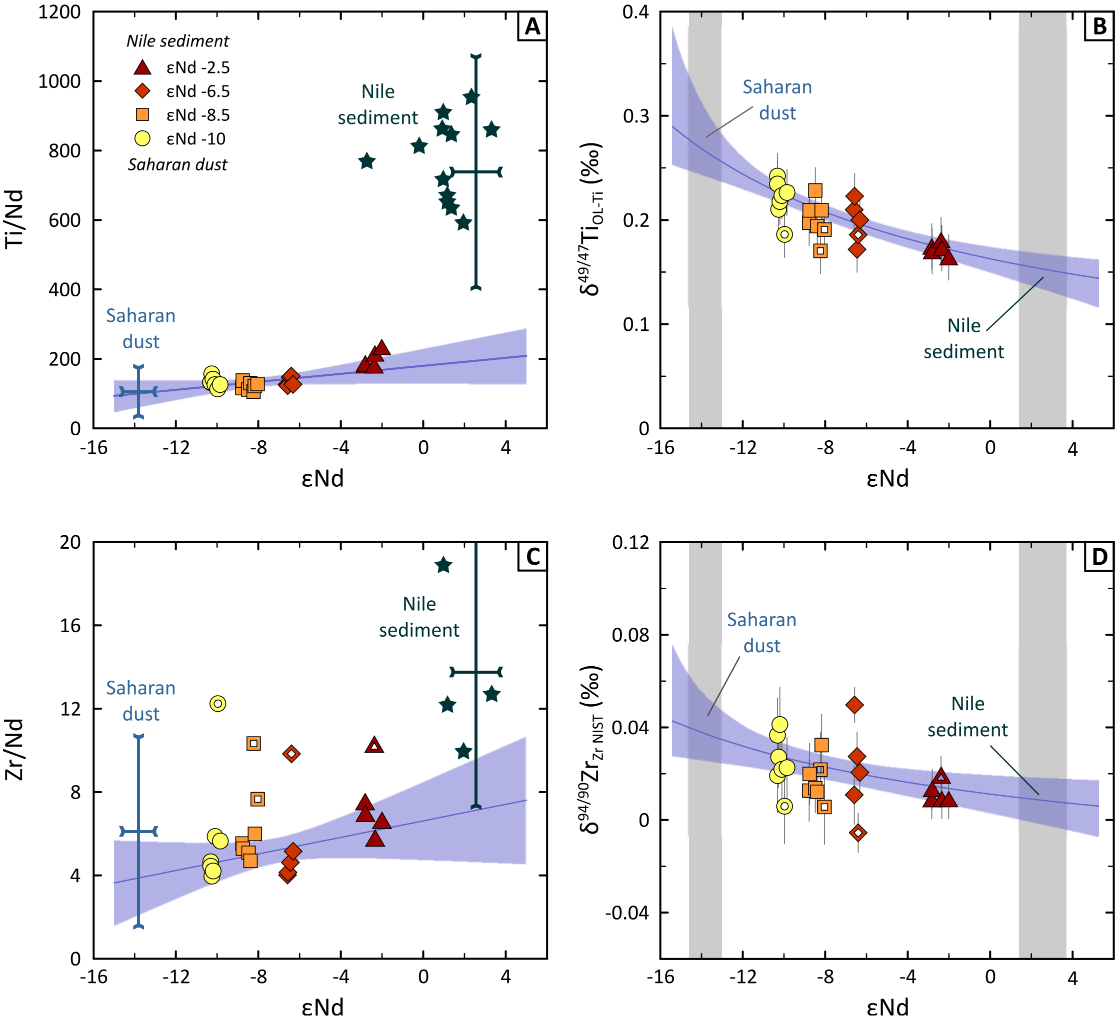

Figure 6. *Composition of the suspended load of the Nile (Garzanti et al., 2015) in relation to the EMS sediments (Klaver et al., 2015). A) Nile suspended sediments display systematic variation in Ti/Nd as a function of grain size fraction, but only the coarsest (125-180 µm) fractions approach the Ti/Nd of EMS sediments. Uncertainties are 1s; Nile sediment data are provided in Supplementary Dataset 1. B) Th/Nb versus La/Nb diagram showing that EMS sediments, which are colour-coded for εNd, are binary mixtures between Saharan dust (low εNd) and a Nile-derived component (high εNd). The <63 µm suspended sediment fraction (uncertainties are 1s) is a good match for this Nile-derived component.*

We regressed the average composition of the four EMS sediment εNd groups (Table 2), excluding samples with negative ΔεHf and/or Zr/Nd >10, in εNd versus Ti/Nd and Zr/Nd space (Figure 5B and D). The composition of Saharan dust compiled from the literature is a good match for the low-εNd component in the EMS sediments for both Ti/Nd and Zr/Nd. There is some Zr/Nd variation between different size fractions of Saharan soils and the finer fractions (<12 µm) tend to have lower Zr/Nd than coarser fractions, likely due to an underrepresentation of zircon in the finest fractions dominated by clay minerals (Castillo et al., 2008). The overall range in Zr/Nd observed in Saharan soils and aerosols overlaps with the range from zircon-enriched to zircon-depleted EMS sediments. The Zr/Nd composition of suspended Nile sediment also agrees well with the high-εNd component in the EMS sediments, but there is a pronounced mismatch for Ti/Nd. Whereas the EMS sediments require a high-εNd mixing component with Ti/Nd of ca. 195, suspended Nile sediment has approximately four times higher Ti/Nd (Figure 5A). A similar offset is observed for other oxide-hosted elements such as V but contrasts with good match between Nile silt and EMS sediments for other trace element ratios such as La/Nb and Th/Nb (Figure 6). The significance of this mismatch is discussed below.

Building on the observations described above, we constrained $\delta^{49/47}$Ti and $\delta^{94/90}$Zr of the provenance components by a regression versus εNd of the EMS sediment sample group averages, again excluding samples with negative ΔεHf. The 95 % confidence envelopes shown in Figure 5 were obtained through a Monte Carlo method using the regressed Ti/Nd and Zr/Nd composition of the mixing components (see supplementary material for more details).

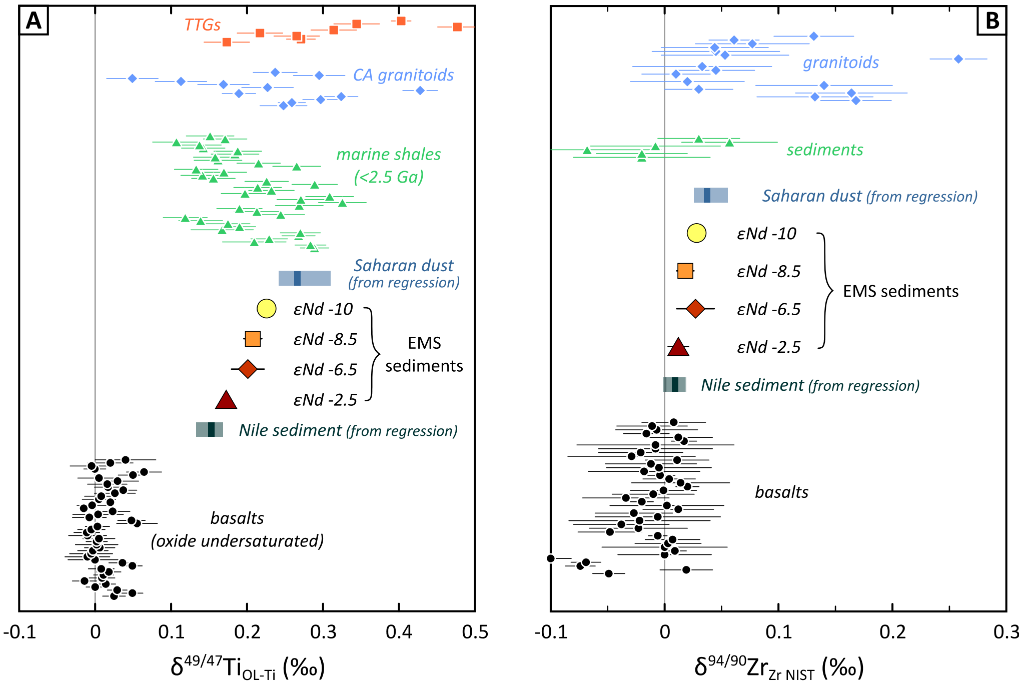

Figure 7. *The Ti–Zr isotope composition of the EMS sediment group averages and the regressed compositions of Saharan dust and Nile sediment. A)* $\delta^{49/47}$*Ti compared with literature data for oxide-undersaturated basalts, Proterozoic to present-day marine shales, calk-alkaline granitoids (60-70 wt.%* SiO_2*) and tonalite-trondhjemite-granodiorite (TTG) suite samples (60-70 wt.%* SiO_2*; Millet and Dauphas, 2014; Millet et al., 2016; Greber et al., 2017; Deng et al., 2018; Deng et al., 2019; Aarons et al., 2020; Hoare et al., 2020). B)* $\delta^{94/90}$*Zr compared with literature data for basalts, granitoids (≥65 wt.%* SiO_2*) and sediments (Inglis et al., 2018; Inglis et al., 2019; Feng et al., 2020; Tian et al., 2020). Two Hekla rhyolites from Inglis et al. (2019) at* $\delta^{94/90}$*Zr ca. 0.5 ‰ fall outside the scale of this figure but are shown in Figure 3.*

5.2.1. Ti–Zr isotope composition of Saharan dust and its protolith

The Saharan dust component was found to have $\delta^{49/47}$Ti = $0.266^{+0.044}_{-0.024}$ ‰ and $\delta^{94/90}$Zr = $0.037^{+0.018}_{-0.011}$ ‰ (Figure 5; see also supplementary Figure S4). As Saharan dust is derived predominantly from Proterozoic granitoids in the Tuareg shield, it is not surprising that its $\delta^{49/47}$Ti matches that of calc-alkaline rocks and tonalite-trondhjemite-granodiorite (TTG) suites (Figure 7; Millet et al., 2016; Greber et al., 2017; Aarons et al., 2020; Hoare et al., 2020). Moreover, $\delta^{49/47}$Ti of Saharan dust overlaps with the upper end of Proterozoic to present-day marine shales, which display rather limited variability with time (Figure 7; Greber et al., 2017; Deng et al., 2019).

More unexpected is the small difference in $\delta^{94/90}$Zr between the mafic Nile-derived component (0.009 ± 0.010 ‰) and felsic Saharan dust ($0.037^{+0.018}_{-0.011}$ ‰; Figure 7; see also supplementary Figure S4). Although there are few constraints at present, the only study of magmatic differentiation to date suggested that, upon zircon saturation, fractional crystallisation can drive residual melts towards notably heavy Zr isotope compositions (ca. 0.5 ‰; Inglis et al., 2019; see Figure 3). As discussed in section 5.1.2, pronounced Zr isotope variation is likely caused by kinetic isotope fractionation in the melt as the equilibrium $\Delta^{94/90}\mathrm{Zr}_{\mathrm{zircon-melt}}$ appears to be close to zero (Chen et al., 2020; Méheut et al., 2021). The $\delta^{94/90}$Zr of Saharan dust is only marginally higher than the regressed Nile-derived component and basalts (Figure 7). This relatively unfractionated signature indicates that the Tuareg Shield granitoids are unlikely to have formed through extensive fractional crystallisation from a mafic parental melt, as that would be conducive to kinetic Zr fractionation effects being recorded in the residual melt (cf., Inglis et al., 2019). Instead, many Neoproterozoic granitoid intrusions in the Tuareg Shield appear to be produced through anatexis of the lower crust (e.g., Liégeois et al., 1994; Abdallah et al., 2007). Although there are at present few constraints, it thus appears that remelting of mafic crust, which likely has $\delta^{94/90}$Zr ≈ 0 ‰ (Figure 7A), at a value for $\Delta^{94/90}\mathrm{Zr}_{\mathrm{zircon-melt}}$ that is close to zero but likely slightly negative (Chen et al., 2020; Méheut et al., 2021) could produce granitoids with only marginally elevated $\delta^{94/90}$Zr. Subsequent cooling at a sufficiently slow rate to maintain Zr isotope equilibrium in the residual melt during zircon growth can then account for the negligible bias in $\delta^{94/90}$Zr introduced by hydrodynamic sorting of zircon in the EMS sediments. Some support for this model is provided by the relatively unfractionated to slightly positive $\delta^{94/90}$Zr (0–0.1 ‰; Figure 7) of an unassorted set of rocks of broadly granitoid composition measured in several Zr isotope methodological studies (Inglis et al., 2018; Feng et al., 2020; Tian et al., 2020), which overlap with the regressed Saharan dust composition.

5.2.2. Titanium isotope fractionation in the Nile system

The Nile-derived component, as found by regression of the EMS sediment samples, has Zr/Nd (7 ± 3) that roughly overlaps with suspended Nile sediment (14 ± 6; Garzanti et al., 2015; see Figure 5) and the Ethiopian flood basalts (e.g., 8 ± 3; Pik et al., 1999; Kieffer et al., 2004) that provide 95 % of the Nile sediment load (Foucault and Stanley, 1989; Padoan et al., 2011; Garzanti et al., 2015). The majority of the Ethiopian flood basalts are undersaturated in zircon and the Zr budget of Nile sediment is hosted mainly in volcanic lithics (Garzanti et al., 2015). Although zircon is present in low abundance in heavy mineral assemblages of Nile sediment, U/Pb dating indicates that it is near-exclusively derived from the Proterozoic crystalline basement of Sudan and Egypt (Garzanti et al., 2018). The Nile-derived component in the EMS sediments has $\delta^{94/90}$Zr of 0.009 ± 0.010 ‰ and thus overlaps with basalts, which cluster around $\delta^{94/90}$Zr = 0 ‰ (Figure 7). Although there are no $\delta^{94/90}$Zr data for the Ethiopian basalts, based on the Zr isotope homogeneity of within-plate basalts (Inglis et al., 2019) it is reasonable to assume that the zircon-undersaturated Ethiopian flood basalts have a similarly unfractionated Zr isotope composition. Hence, the lack of $\delta^{94/90}$Zr fractionation from source to sink indicates that the minor enrichment in Zr of silt-sized Nile sediment fractions and potential hydrodynamic sorting of zircon and baddeleyite in the sedimentary system of the Nile fractions cause no detectable shift in $\delta^{94/90}$Zr.

Titanium forms a different case. The regressed Ti/Nd of the Nile-derived component in the EMS sediments is notably lower (195^{+78}_{-64}; see Table 2) than both suspended Nile sediment (ca. 740 ± 330; Garzanti et al., 2015) and Ethiopian flood basalts (ca. 610 ± 200; Pik et al., 1999; Kieffer et al., 2004; Field et al., 2013; see Figure 8). In addition, $\delta^{49/47}$Ti of the Nile-derived component ($0.153^{+0.015}_{-0.020}$ ‰) is clearly fractionated relative to oxide-undersaturated basalts, which have $\delta^{49/47}$Ti in a narrow window close to zero (e.g., Millet et al., 2016; Deng et

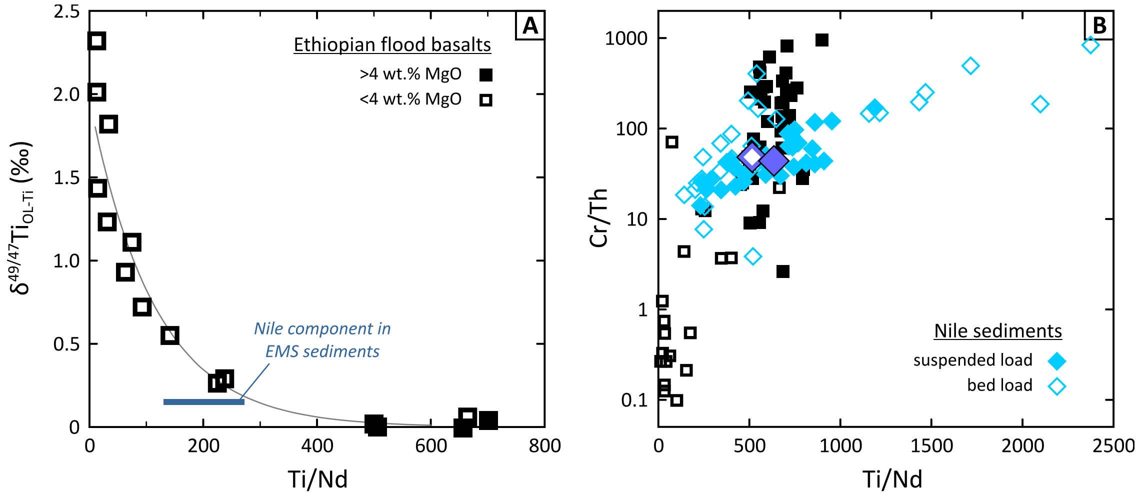

Figure 8. *Constraints on the protolith of Nile sediments. A) Ti/Nd versus* $\delta^{49/47}$*Ti of the regressed Nile-derived component in the EMS sediments (blue bar; see Figure 5) in comparison with data for Ethiopian flood basalts (Deng et al., 2019; Hoare et al., 2020). The thin grey line is a regression of the basalt data. B) Ti/Nd versus Cr/Th diagram illustrating that oxide-undersaturated basalts are the dominant component of Nile sediments. Ethiopian flood basalts (Pik et al., 1998; Pik et al., 1999; Field et al., 2013) with <4 wt.% MgO and fractionated* $\delta^{49/47}$*Ti have distinctly lower Cr/Th than both suspended load and bed load Nile sediments (Garzanti et al., 2015). Median compositions for suspended load and bed load are shown by the larger diamonds in a darker shade of blue. See text for further discussion.*

al., 2018; Johnson et al., 2019; see Figure 3). Titanium isotope data are available for the Ethiopian flood basalts as both Deng et al. (2019) and Hoare et al. (2020) measured cogenetic suites of samples from the Afar region of the flood basalt province. Primitive Afar samples have $\delta^{49/47}$Ti of 0.014 ± 0.021 ‰ but, upon saturation in titanomagnetite and ilmenite at ca. 4 wt.% MgO, Ti/Nd decreases and $\delta^{49/47}$Ti rapidly increases up to +2.5 ‰ in the most evolved rhyolitic samples (Figure 8).

It might be tempting to ascribe the low Ti/Nd and elevated $\delta^{49/47}$Ti of the Nile-derived component in the EMS sediments to the weathering of evolved, isotopically fractionated lavas (cf., Deng et al., 2019). The $\delta^{49/47}$Ti distribution in Afar samples shown in Figure 8 is, however, strongly skewed towards highly evolved melt compositions as Deng et al. (2019) and Hoare et al. (2020) specifically targeted evolved samples to investigate the effects of fractional crystallisation of Fe-Ti oxides on $\delta^{49/47}$Ti. Such evolved lavas are a volumetrically minor component of the flood basalt province and are thus unlikely to be a significant source of erodible material. Less evolved lavas (>4 wt.% MgO) with unfractionated $\delta^{49/47}$Ti at the bulk rock scale and higher TiO_2 contents are far more abundant and dominate the Ti budget available for weathering. Indeed, Nile sediments have Ti/Nd overlapping with oxide-undersaturated Afar basalts (Figure 8A), which argues against preferential weathering of isotopically heavy, evolved lavas with lower Ti/Nd. Additional support is provided by comparing Ti/Nd with trace element ratios that are insensitive to the fractional crystallisation of Fe-Ti oxides, such as Cr/Th. As Cr/Th decreases during magmatic differentiation, due to the compatibility of Cr in clinopyroxene and spinel whereas Th is highly incompatible, evolved Afar basalts with <4 wt.% MgO have lower Cr/Th than both suspended load and bed load Nile sediments (Figure 8B). Hence, the offset in Cr/Th is unlikely to result from sorting by grain size and reflects the primitive nature of the protolith of Nile sediments, even if Ti/Nd in silt-sized fractions is slightly elevated due to concentration of Fe-Ti oxides (Figure 6). The Cr/Th composition of Nile sediments constrains the proportion of evolved lavas with high $\delta^{49/47}$Ti in the sediment budget to be <20 %, which is insufficient to bring $\delta^{49/47}$Ti into agreement with the regressed Nile-derived component ($\delta^{49/47}$Ti = $0.153^{+0.015}_{-0.020}$ ‰; Figure 5). As a result, there is convincing evidence that oxide-undersaturated basalts with $\delta^{49/47}$Ti close to zero are the dominant source of Ti in Nile sediments. These less evolved lavas, however, are very likely to contain isotopically light oxides that crystallised during cooling of the lava flows, which are balanced by an isotopically heavier groundmass to yield a bulk composition with $\delta^{49/47}$Ti of zero. Overrepresentation of these oxides might cause silt-sized suspended Nile sediments to have slightly negative $\delta^{49/47}$Ti, and hence clearly cannot account for the distinctly positive Ti isotope composition of the regressed Nile-derived component in the EMS sediments.

There is no evidence for pronounced Ti/Nd fractionation during weathering and fluvial transport in the Nile. No clear downstream trend in Ti/Nd can be observed in suspended Nile sediment and samples in Garzanti et al. (2015) taken furthest downstream, at the third cataract close to the Aswan dam, still have Ti/Nd of ca. 600. Despite their higher density compared to silicate minerals, Fe-Ti oxides do not appear to settle out and heavy mineral assemblages are carried in essentially unmodified concentration and composition from their source to the delta (Garzanti et al., 2015).

The mismatch in Ti/Nd, and by inference $\delta^{49/47}$Ti, between suspended Nile sediment and the Nile-derived component recorded in the EMS sediments is most likely the result of large-scale loss of Fe-Ti oxides in the littoral cell of the Nile. Upon entering the EMS, Nile sediment is transported eastward along the coast of Egypt and the Levant (e.g., Pomerancblum, 1966; Goldsmith and Golik, 1980; see Figure 2). The proportion of heavy minerals decreases rapidly east of the Nile delta and Fe-Ti oxides are concentrated in beach sands (Garzanti et al., 2015), of which almost pure Fe-Ti oxide placer deposits (e.g., the Rosetta and Damietta placer deposits; Frihy, 2007; Abdel-Karim et al., 2016) are an extreme manifestation. Retention of isotopically light Fe-Ti oxides in near-shore deposits will bias the composition of Nile sediment that is transported further into the EMS to higher $\delta^{49/47}$Ti and lower Ti/Nd, which is our preferred explanation for the elevated $\delta^{49/47}$Ti of the Nile-derived high-εNd component recorded in the EMS sediments. Assuming that suspended Nile sediment has similar $\delta^{49/47}$Ti to the oxide-undersaturated Afar basalts (+0.014 ± 0.021 ‰; Deng et al., 2019; Hoare et al., 2020), it follows from mass balance that $\delta^{49/47}$Ti of Fe-Ti oxides in the placer deposits is roughly -0.1 ‰ (Figure 9A).

5.3. Is the sedimentary record a reliable proxy for crustal composition?

5.3.1. Zr isotope composition

Hydrodynamic sorting of zircon barely leaves a trace in $\delta^{94/90}$Zr of the EMS sediment samples (Figure 4), nor is there any evidence for Zr isotope fractionation during weathering or transport. From the limited $\delta^{94/90}$Zr variability, we conclude that zircon has only marginally lower $\delta^{94/90}$Zr than bulk sediments, which is caused by a small $\Delta^{94/90}\mathrm{Zr}_{\mathrm{zircon-melt}}$ and lack of significant kinetic Zr isotope fractionation in the Saharan dust protolith. Moreover, the regressed Nile-derived component in the EMS sediments is unfractionated in terms of Zr/Nd and $\delta^{94/90}$Zr relative to the Ethiopian flood basalts. In the case of the EMS sediments, the fine-grained, zircon-depleted samples thus preserve an unbiased record of the Zr isotope composition of their protoliths. The lack of a clear contrast in $\delta^{94/90}$Zr between felsic Saharan dust and mafic Nile sediment, however, means that Zr isotopes in this case offer little resolution as a provenance indicator and, by implication, as a proxy for crustal composition.

It is unclear to what extent this observation can be generalised. Kinetic fractionation effects are commonly observed in natural zircon from a variety of tectonic settings (Ibañez-Mejia and Tissot, 2019; Zhang et al., 2019; Guo et al., 2020). Hydrodynamic sorting of such isotopically fractionated zircon could impose a large bias in $\delta^{94/90}$Zr in fine-grained sediments. As zircon can have both strongly positive and negative $\delta^{94/90}$Zr, depending on the crystallisation mode and direction of Zr diffusion in the melt (Chen et al., 2020; Méheut et al., 2021), predicting the sign and magnitude of a zircon effect on fine-grained sediments might be difficult. More Zr isotope data for sediments as well as magmatic differentiation suites are needed to better understand Zr isotope fractionation in igneous rocks and the sedimentary cycle in order to evaluate the potential of Zr isotopes as a provenance tracer or as a proxy for the average composition of the erodible continental crust through time.

5.3.2. Titanium isotopes and the "oxide effect"

The EMS sediments provide an example of how the removal of Fe-Ti rich oxides through hydrodynamic sorting in a near-shore environment may shift the $\delta^{49/47}$Ti isotope composition of the remaining fine-grained sediment fraction to higher values. The limited variation in $\delta^{49/47}$Ti and TiO_2/Al_2O_3 in EMS sediments with the strongest Nile signature (εNd -2.5; see Figure 4) left few clues to the large isotopic bias introduced by hydrodynamic sorting of oxides. The magnitude of the shift in $\delta^{49/47}$Ti could only be unravelled through the well-established framework of EMS sediment provenance and the availability of geochemical data for suspended Nile sediment. This raises

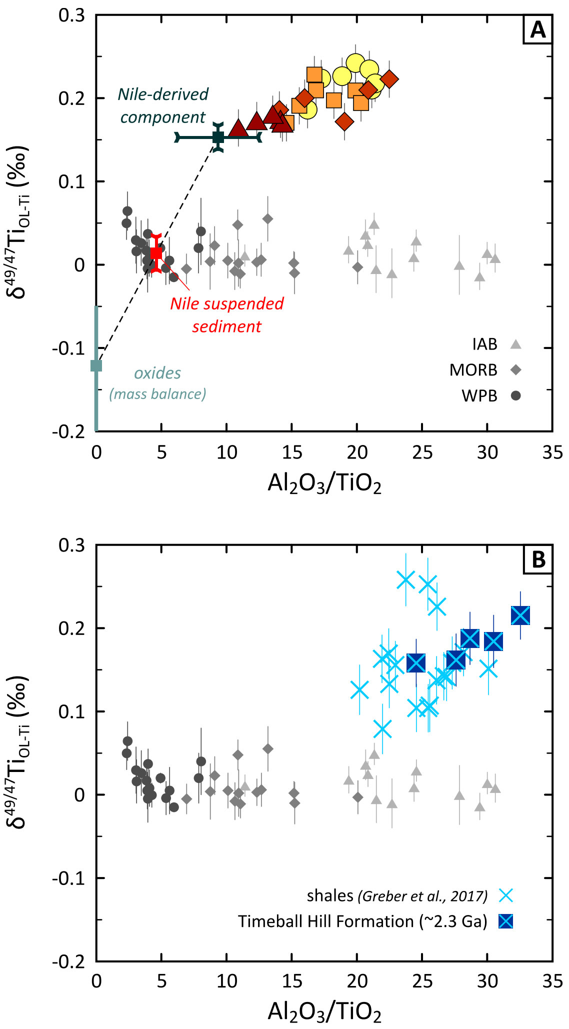

Figure 9. *The "oxide effect" on $\delta^{49/47}$Ti of the EMS sediments (symbols for EMS sediments as in previous figures). A) Al_2O_3/TiO_2 versus $\delta^{49/47}$Ti diagram showing how hydrodynamic sorting of isotopically light Fe-Ti oxides can shift the composition of suspended Nile sediment (in red) towards the Nile-derived component recorded in the EMS sediments (see Figure 5). Suspended Nile sediment is assumed to have the same $\delta^{49/47}$Ti as Afar basalts with >4 wt.% MgO (0.014 ± 0.021 ‰; Deng et al., 2019; Hoare et al., 2020). For comparison, the variation in Al_2O_3/TiO_2 and $\delta^{49/47}$Ti of island arc basalts (IAB), mid-ocean ridge basalts (MORB) and within-plate basalts (WPB) is shown (Millet and Dauphas, 2014; Millet et al., 2016; Deng et al., 2018; Deng et al., 2019; Hoare et al., 2020); B) Covariation between Al_2O_3/TiO_2 and $\delta^{49/47}$Ti in shales that are used to estimate average upper crustal compositions through time (Greber et al., 2017). A set of five samples from the same locality (Timeball Hill Formation, South Africa) is highlighted; see text for discussion.*

the question of how common this "oxide effect" could be in the sedimentary record, and to what extent it can have biased estimates of the composition of the erodible crust that are based on $\delta^{49/47}$Ti of shales (Greber et al., 2017; Deng et al., 2019).

A first constraint comes from the relatively common occurrence of placer deposits rich in magnetite, ilmenite, and rutile in near-shore environments around the globe, both in modern sediments and in the rock record, that can form economically viable sources of Ti (e.g., Komar and Wang, 1984; Paine et al., 2005; Bernstein et al., 2008; Garçon et al., 2011; Lalomov et al., 2015). Although such placer deposits are a volumetrically minor sink for Fe-Ti oxides, their common occurrence does showcase the general potential for notable loss of Fe-Ti oxides through hydrodynamic sorting in deltas and other near-shore environments. As a result, it is possible that hydrodynamic sorting can have been a factor modulating $\delta^{49/47}$Ti of global marine sediments throughout Earth's history. The mode and degree of weathering, however, can influence if and to what extent hydrodynamic sorting of Fe-Ti oxides can occur. Fine-grained Nile sediments are for >95 % derived from the Ethiopian Highlands where the high relief and strongly seasonal rainfall and run-off mean that physical weathering is dominant (Garzanti et al., 2015). As a result, Ti-rich oxides are transported essentially unaltered from their source to the Nile delta (Abdel-Karim et al., 2016). Ilmenite, rutile, and, to a lesser extent, titanomagnetite are durable and little affected by mechanical abrasion and alteration. Strong chemical weathering does seem to drive recrystallisation of Fe-Ti oxides as more labile Fe is removed from their structure, which can be associated with a reduction in grain size (e.g., Morad and Adin Aldahan, 1986; Basu and Molinaroli, 1989), but does not appear to cause notable Ti isotope fractionation (Heard et al., 2021). Hence, chemical weathering under oxidising conditions might allow Fe-Ti oxides to be transported in the clay mineral fraction and escape hydrodynamic sorting.

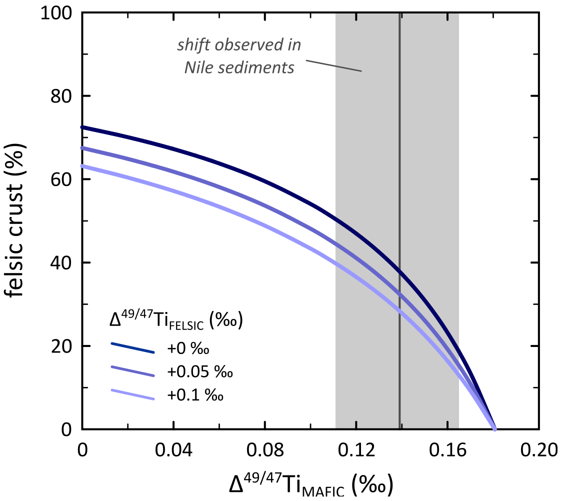

Figure 10. *Potential bias in the model of Greber et al. (2017) for the proportion of felsic crust recorded in present-day shales ($\delta^{49/47}Ti$ = 0.186 ‰) due to an "oxide effect". For simplicity, we ignore the negligible contribution of Ti from komatiites to present-day shales and only consider the bias that is introduced by shifting the composition of the mafic ($\Delta^{49/47}Ti_{MAFIC}$) and felsic ($\Delta^{49/47}Ti_{FELSIC}$) mixing components through hydrodynamic sorting of isotopically light Fe-Ti oxides. See text for discussion.*

Greber and Dauphas (2019) investigated Al_2O_3/TiO_2 of the shale and diamictite records to gauge the effects of hydrodynamic sorting of Fe-Ti oxides through time. Based on the general homogeneity of Al_2O_3/TiO_2, they suggested that sorting of Fe-Ti oxides is of minor influence in comparison with the more pronounced zircon effect recorded in those sediment records. Our new data show, however, that the magnitude of Ti isotope fractionation caused by Fe-Ti oxide loss can be significant. In Nile sediments, it causes a ca. 0.14 ‰ increase in $\delta^{49/47}Ti$ while Al_2O_3/TiO_2 only shows a modest increase (from ca. 5 to ca. 9; Figure 9A) relative to the variation observed in basalts from different tectonic settings. The latter all have $\delta^{49/47}Ti$ near zero but show a systematic increase in Al_2O_3/TiO_2 from alkaline within-plate basalts (WPB) to tholeiitic mid-ocean ridge basalts (MORB) and calc-alkaline island arc basalts (IAB; Figure 9). Hydrodynamic sorting of oxides in the Nile does not shift Al_2O_3/TiO_2 outside the range of basalts and, as such, cannot be detected on the basis of Al_2O_3/TiO_2 alone.

The potential of a ca. 0.14 ‰ shift in $\delta^{49/47}Ti$ in fine-grained sediments derived from mafic sources, such as observed in Nile sediment, has important ramifications for the use of Ti isotopes in detrital sediments as a proxy for upper crustal compositions. For example, Greber et al. (2017) use a Ti isotope mass balance where the mafic component is anchored at $\delta^{49/47}Ti$ = +0.005 ‰ (the bulk silicate Earth value of Millet et al., 2016) to derive a proportion of ca. 72 % felsic crust based on composition of present-day shales ($\delta^{49/47}Ti$ = 0.186 ‰). Increasing $\delta^{49/47}Ti$ of the mafic endmember in that mass balance calculation by 0.14 ‰, while keeping all other parameters the same, leads to a decrease in the calculated proportion of felsic crust to just 37 % (Figure 10). A concomitant decrease in the Ti content of the mafic endmember, or positive shift in $\delta^{49/47}Ti$ of the felsic endmember through loss of isotopically light Fe-Ti oxides, would further lower the calculated proportion of felsic crust recorded in present-day shales (Figure 10).

Taken at face value, an increase in $\delta^{49/47}Ti$ of fine-grained sediments through hydrodynamic sorting of Fe-Ti oxides can thus lead to gross overestimation of the proportion of felsic rocks exposed in the continental crust. The example above is, however, an extreme scenario and there is abundant independent evidence, both from elemental systematics of shales, loess, and diamictites and from mapping of the proportion of felsic rocks exposed at Earth's surface (e.g., Taylor and McLennan, 1985; Condie, 1993; Tang et al., 2016; Greber and Dauphas, 2019), that the $\delta^{49/47}Ti$-based present-day estimate of 72 % felsic crust by Greber et al. (2017) is reasonably accurate. Hence, the actual $\delta^{49/47}Ti$ bias introduced in the detrital sediment record by an oxide effect is likely smaller. Although it is plausible that hydrodynamic sorting has affected the riverine Ti budget through time, we do not observe noticeable loss of Ti-rich oxides in the Saharan dust component. Aeolian dust, which can constitute up to 50 % of total sediment budget delivered to the deep oceans (e.g., Pye, 1987), may thus be affected less by the loss of isotopically light Fe-Ti oxides. Nevertheless, at least part of the scatter in the shale samples used by Greber et al. (2017) and Deng et al. (2019) to estimate the average crustal composition through time (Figure 7) could be attributed to an oxide effect. With a single exception, Greber et al. (2017) report data for only one or two samples per locality, which makes it difficult to evaluate the possibility of a bias on $\delta^{49/47}$Ti introduced by hydrodynamic sorting of Fe-Ti oxides (Figure 9B). The exception is the ca. 2.3 Ga Timeball Hill Formation (South Africa) for which five samples have been measured. These have been highlighted in Figure 9B and do show a clear positive correlation between Al_2O_3/TiO_2 and $\delta^{49/47}$Ti, suggesting that sorting of oxides might be responsible for at least for part of the $\delta^{49/47}$Ti variation within that formation and, by inference, the shale record. To better understand the potential bias imparted by hydrodynamic sorting of Fe-Ti oxides, it would be useful to compare the shale record to diamictites, which might be less affected by this process (Gaschnig et al., 2016; Greber and Dauphas, 2019).

6. Conclusions

We measured a suite of well-characterised sediments from the Eastern Mediterranean Sea (EMS) for their Ti and Zr isotope compositions to investigate the effect of hydrodynamic sorting on Ti–Zr isotope systematics. Previous work has established that the EMS sediments are binary mixtures of felsic Saharan dust and mafic Nile-derived sediments. The samples display a clear geochemical signature of zircon accumulation and depletion as the result of hydrodynamic sorting. Titanium was found to concentrate in tandem with, but to a smaller extent than Zr within the studied EMS sediment samples. As to the isotopic effects of hydrodynamic sorting of Fe-Ti oxides and zircon, we can conclude the following:

1) The most oxide- and zircon-enriched samples have marginally lower $\delta^{49/47}$Ti and $\delta^{94/90}$Zr than fine-grained samples, but in general the $\delta^{49/47}$Ti and $\delta^{94/90}$Zr variations observed in our dataset are limited. In the case of Zr, fine-grained EMS sediments appear to accurately reflect the $\delta^{94/90}$Zr of their protolith and no significant bias is introduced by the hydrodynamic sorting of zircon or baddeleyite.
2) Regression of the EMS sediment samples reveals that the felsic Saharan dust provenance component has only marginally (ca. 0.03 ‰) higher $\delta^{94/90}$Zr than basalts. Together with the lack of pronounced $\delta^{94/90}$Zr variation imparted by hydrodynamic sorting of zircon, this suggests negligible zircon-melt Zr isotope fractionation has occurred in the Saharan dust protolith. This is consistent with theoretical models that argue for $\Delta^{94/90}Zr_{zircon–melt}$ close to zero and suggests that the large Zr isotope heterogeneity observed in natural zircon and volcanic rocks might not be a ubiquitous feature of igneous rocks.
3) Based on the limited spread in $\delta^{94/90}$Zr between mafic Nile sediments and felsic Saharan dust, Zr isotope systematics of detrital sediments appear to lack sufficient resolution to be a promising tracer of crustal composition.
4) Saharan dust has $\delta^{49/47}$Ti of $0.266^{+0.044}_{-0.024}$ ‰ as estimated through regression of the EMS sediment samples, which is similar to calc-alkaline granitoids, TTGs and average Proterozoic and Phanerozoic shales.
5) The Nile-derived component in the EMS sediments has notably higher $\delta^{49/47}$Ti and lower Ti/Nd than its protolith – the Ethiopian flood basalts. Although detritus of these basalts is carried essentially unmodified to the delta, large-scale loss of isotopically light Fe-Ti oxides in the littoral cell of the Nile shifts $\delta^{49/47}$Ti of the remaining suspended sediment fraction by +0.14 ‰.
6) The consequences of such an "oxide effect" can be cryptic and not readily discernible from major- or trace element systematics of fine-grained sediments alone, or from the study of isolated samples from different sedimentary units. Its influence on $\delta^{49/47}$Ti, however, can be pronounced and it can translate into a significant bias in average upper crustal composition estimates based on $\delta^{49/47}$Ti of the detrital shale record. We propose that the notable scatter in $\delta^{49/47}$Ti of shales is likely to be caused, at least in part, by such an oxide effect.

Acknowledgements

The EMS sediment samples were kindly provided by the DSPD/ODP core repository in Bremen. We thank Liam Hoare for assistance in the lab, Chris Coath for providing the code for some of the regressions and Zhengbin Deng for sharing Nd concentration data for several Afar samples. Careful reviews by Zhengbin Deng and three anonymous reviewers helped improve the paper. Associate editor James Day is thanked for efficient handling of the manuscript. This work was supported by NERC Standard grant NE/R001332/1 and a Royal Society Research Grant to MAM, NSF-EAR grants 1823748 (to MIM) and 1824002 (to FLHT), as well as start-up funds to FLHT provided by Caltech.

References

Aarons, S.M., Reimink, J.R., Greber, N.D., Heard, A.W., Zhang, Z. and Dauphas, N. (2020) Titanium isotopes constrain a magmatic transition at the Hadean-Archean boundary in the Acasta Gneiss Complex. *Science Advances* **6**, eabc9959.

Abdallah, N., Liégeois, J.-P., De Waele, B., Fezaa, N. and Ouabadi, A. (2007) The Temaguessine Fe-cordierite orbicular granite (Central Hoggar, Algeria): U–Pb SHRIMP age, petrology, origin and geodynamical consequences for the late Pan-African magmatism of the Tuareg shield. *J. Afr. Earth Sci.* **49**, 153-178.

Abdel-Karim, A.-A.M., Zaid, S.M., Moustafa, M.I. and Barakat, M.G. (2016) Mineralogy, chemistry and radioactivity of the heavy minerals in the black sands, along the northern coast of Egypt. *J. Afr. Earth Sci.* **123**, 10-20.

Bartolini, C., Malesani, P., Manetti, P. and Wezel, F.C. (1975) Sedimentology and petrology of Quaternary sediments from the Hellenic Trench, Mediterranean Ridge and the Nile Cone from DSDP, Leg 13, cores. *Sedimentology* **22**, 205-236.

Basu, A. and Molinaroli, E. (1989) Provenance characteristics of detrital opaque Fe-Ti oxide minerals. *J. Sediment. Res.* **59**, 922-934.

Bayon, G., Burton, K., Soulet, G., Vigier, N., Dennielou, B., Etoubleau, J., Ponzevera, E., German, C. and Nesbitt, R. (2009) Hf and Nd isotopes in marine sediments: Constraints on global silicate weathering. *Earth Planet. Sci. Lett.* **277**, 318-326.

Bayon, G., Toucanne, S., Skonieczny, C., André, L., Bermell, S., Cheron, S., Dennielou, B., Etoubleau, J., Freslon, N. and Gauchery, T. (2015) Rare earth elements and neodymium isotopes in world river sediments revisited. *Geochim. Cosmochim. Acta* **170**, 17-38.

Bernstein, S., Frei, D., McLimans, R.K., Knudsen, C. and Vasudev, V.N. (2008) Application of CCSEM to heavy mineral deposits: Source of high-Ti ilmenite sand deposits of South Kerala beaches, SW India. *J. Geochem. Explor.* **96**, 25-42.

Bouvier, A., Vervoort, J.D. and Patchett, P.J. (2008) The Lu–Hf and Sm–Nd isotopic composition of CHUR: Constraints from unequilibrated chondrites and implications for the bulk composition of terrestrial planets. *Earth Planet. Sci. Lett.* **273**, 48-57.

Carpentier, M., Chauvel, C. and Mattielli, N. (2008) Pb–Nd isotopic constraints on sedimentary input into the Lesser Antilles arc system. *Earth Planet. Sci. Lett.* **272**, 199-211.

Carpentier, M., Chauvel, C., Maury, R.C. and Mattielli, N. (2009) The "zircon effect" as recorded by the chemical and Hf isotopic compositions of Lesser Antilles forearc sediments. *Earth Planet. Sci. Lett.* **287**, 86-99.

Castillo, S., Moreno, T., Querol, X., Alastuey, A., Cuevas, E., Herrmann, L., Mounkaila, M. and Gibbons, W. (2008) Trace element variation in size-fractionated African desert dusts. *J. Arid Environ.* **72**, 1034-1045.

Chen, X., Wang, W., Zhang, Z., Nie, N.X. and Dauphas, N. (2020) Evidence from Ab Initio and Transport Modeling for Diffusion-Driven Zirconium Isotopic Fractionation in Igneous Rocks. *ACS Earth and Space Chemistry* **4**, 1572-1595.

Condie, K.C. (1993) Chemical composition and evolution of the upper continental crust: contrasting results from surface samples and shales. *Chem. Geol.* **104**, 1-37.

Coplen, T.B. (2011) Guidelines and recommended terms for expression of stable-isotope-ratio and gas-ratio measurement results. *Rapid communications in mass spectrometry* **25**, 2538-2560.

Deng, Z., Moynier, F., Sossi, P. and Chaussidon, M. (2018) Bridging the depleted MORB mantle and the continental crust using titanium isotopes. *Geochemical Perspectives Letters* **9**, 11-15.

Deng, Z., Chaussidon, M., Savage, P., Robert, F., Pik, R. and Moynier, F. (2019) Titanium isotopes as a tracer for the plume or island arc affinity of felsic rocks. *Proceedings of the National Academy of Sciences* **116**, 1132-1135.

Feng, L., Hu, W., Jiao, Y., Zhou, L., Zhang, W., Hu, Z. and Liu, Y. (2020) High-precision stable zirconium isotope ratio measurements by double spike thermal ionization mass spectrometry. *J. Anal. At. Spectrom.* **35**, 736-745.

Field, L., Blundy, J., Calvert, A. and Yirgu, G. (2013) Magmatic history of Dabbahu, a composite volcano in the Afar Rift, Ethiopia. *Bulletin* **125**, 128-147.

Foucault, A. and Stanley, D.J. (1989) Late Quaternary palaeoclimatic oscillations in East Africa recorded by heavy minerals in the Nile delta. *Nature* **339**, 44-46.

Frihy, O.E. (2007) The Nile Delta: processes of heavy mineral sorting and depositional patterns. *Dev. Sedimentol.* **58**, 49-74.

Garçon, M. and Chauvel, C. (2014) Where is basalt in river sediments, and why does it matter? *Earth Planet. Sci. Lett.* **407**, 61-69.

Garçon, M., Chauvel, C. and Bureau, S. (2011) Beach placer, a proxy for the average Nd and Hf isotopic composition of a continental area. *Chem. Geol.* **287**, 182-192.

Garçon, M., Chauvel, C., France-Lanord, C., Huyghe, P. and Lavé, J. (2013) Continental sedimentary processes decouple Nd and Hf isotopes. *Geochim. Cosmochim. Acta* **121**, 177-195.

Garzanti, E., Andò, S., Padoan, M., Vezzoli, G. and El Kammar, A. (2015) The modern Nile sediment system: Processes and products. *Quat. Sci. Rev.* **130**, 9-56.

Garzanti, E., Vermeesch, P., Rittner, M. and Simmons, M. (2018) The zircon story of the Nile: Time-structure maps of source rocks and discontinuous propagation of detrital signals. *Basin Res.* **30**, 1098-1117.

Gaschnig, R.M., Rudnick, R.L., McDonough, W.F., Kaufman, A.J., Valley, J.W., Hu, Z., Gao, S. and Beck, M.L. (2016) Compositional evolution of the upper continental crust through time, as constrained by ancient glacial diamictites. *Geochim. Cosmochim. Acta* **186**, 316-343.

Goldsmith, V. and Golik, A. (1980) Sediment transport model of the southeastern Mediterranean coast. *Mar. Geol.* **37**, 147-175.

Goudie, A. and Middleton, N. (2001) Saharan dust storms: nature and consequences. *Earth-Science Reviews* **56**, 179-204.

Greber, N.D. and Dauphas, N. (2019) The chemistry of fine-grained terrigenous sediments reveals a chemically evolved Paleoarchean emerged crust. *Geochim. Cosmochim. Acta* **255**, 247-264.

Greber, N.D., Dauphas, N., Bekker, A., Ptáček, M.P., Bindeman, I.N. and Hofmann, A. (2017) Titanium isotopic evidence for felsic crust and plate tectonics 3.5 billion years ago. *Science* **357**, 1271-1274.

Grousset, F.E. and Biscaye, P.E. (2005) Tracing dust sources and transport patterns using Sr, Nd and Pb isotopes. *Chem. Geol.* **222**, 149-167.

Grousset, F., Biscaye, P., Zindler, A., Prospero, J. and Chester, R. (1988) Neodymium isotopes as tracers in marine sediments and aerosols: North Atlantic. *Earth Planet. Sci. Lett.* **87**, 367-378.

Grousset, F., Henry, F., Minster, J. and Monaco, A. (1990) Nd isotopes as tracers in water column particles: the western Mediterranean Sea. *Mar. Chem.* **30**, 389-407.

Grousset, F., Rognon, P., Coudé-Gaussen, G. and Pédemay, P. (1992) Origins of peri-Saharan dust deposits traced by their Nd and Sr isotopic composition. *Palaeogeog. Palaeoclimatol. Palaeoecol.* **93**, 203-212.

Grousset, F.E., Parra, M., Bory, A., Martinez, P., Bertrand, P., Shimmield, G. and Ellam, R.M. (1998) Saharan wind regimes traced by the Sr–Nd isotopic composition of subtropical Atlantic sediments: Last Glacial Maximum vs today. *Quat. Sci. Rev.* **17**, 395-409.

Guo, J.-L., Wang, Z., Zhang, W., Moynier, F., Cui, D., Hu, Z. and Ducea, M.N. (2020) Significant Zr isotope variations in single zircon grains recording magma evolution history. *Proceedings of the National Academy of Sciences* **117**, 21125-21131.

Heard, A.W., Aarons, S.M., Hofmann, A., He, X., Ireland, T., Bekker, A., Qin, L. and Dauphas, N. (2021) Anoxic continental surface weathering recorded by the 2.95 Ga Denny Dalton Paleosol (Pongola Supergroup, South Africa). *Geochim. Cosmochim. Acta* **295**, 1-23.

Henry, F., Jeandel, C., Dupre, B. and Minster, J.-F. (1994) Particulate and dissolved Nd in the western Mediterranean Sea: sources, fate and budget. *Mar. Chem.* **45**, 283-305.

Hoare, L., Klaver, M., Saji, N.S., Gillies, J., Parkinson, I.J., Lissenberg, C.J. and Millet, M.-A. (2020) Melt chemistry and redox conditions control titanium isotope fractionation during magmatic differentiation. *Geochim. Cosmochim. Acta* **282**, 38-54.

Ibañez-Mejia, M. and Tissot, F.L. (2019) Extreme Zr stable isotope fractionation during magmatic fractional crystallization. *Science Advances* **5**, eaax8648.

Inglis, E.C., Creech, J.B., Deng, Z. and Moynier, F. (2018) High-precision zirconium stable isotope measurements of geological reference materials as measured by double-spike MC-ICPMS. *Chem. Geol.* **493**, 544-552.

Inglis, E.C., Moynier, F., Creech, J., Deng, Z., Day, J.M., Teng, F.-Z., Bizzarro, M., Jackson, M. and Savage, P. (2019) Isotopic fractionation of zirconium during magmatic differentiation and the stable isotope composition of the silicate Earth. *Geochim. Cosmochim. Acta* **250**, 311-323.

Johnson, A.C., Aarons, S.M., Dauphas, N., Nie, N.X., Zeng, H., Helz, R.T., Romaniello, S.J. and Anbar, A.D. (2019) Titanium isotopic fractionation in Kilauea Iki lava lake driven by oxide crystallization. *Geochim. Cosmochim. Acta* **264**, 180-190.

Kieffer, B., Arndt, N., Lapierre, H., Bastien, F., Bosch, D., Pecher, A., Yirgu, G., Ayalew, D., Weis, D. and Jerram, D.A. (2004) Flood and shield basalts from Ethiopia: magmas from the African superswell. *J. Petrol.* **45**, 793-834.

Klaver, M., Djuly, T., de Graaf, S., Sakes, A., Wijbrans, J., Davies, G. and Vroon, P. (2015) Temporal and spatial variations in provenance of Eastern Mediterranean Sea sediments: Implications for Aegean and Aeolian arc volcanism. *Geochim. Cosmochim. Acta* **153**, 149-168.

Komar, P.D. and Wang, C. (1984) Processes of selective grain transport and the formation of placers on beaches. *The Journal of Geology* **92**, 637-655.

Lalomov, A., Platonov, M., Tugarova, M., Bochneva, A. and Chefranova, A. (2015) Rare metal–titanium placer metal potential of Cambrian–Ordovician sandstones in the northwestern Russian Plate. *Lithol. Mineral Resour.* **50**, 501-511.

Liégeois, J.-P., Black, R., Navez, J. and Latouche, L. (1994) Early and late Pan-African orogenies in the Air assembly of terranes (Tuareg Shield, Niger). *Precambrian Res.* **67**, 59-88.

McLennan, S., Taylor, S., McCulloch, M. and Maynard, J. (1990) Geochemical and Nd-Sr isotopic composition of deep-sea turbidites: crustal evolution and plate tectonic associations. *Geochim. Cosmochim. Acta* **54**, 2015-2050.

Méheut, M., Ibañez-Mejia, M. and Tissot, F.L. (2021) Drivers of zirconium isotope fractionation in Zr-bearing phases and melts: The roles of vibrational, nuclear field shift and diffusive effects. *Geochim. Cosmochim. Acta* **292**, 217-234.

Millet, M.-A. and Dauphas, N. (2014) Ultra-precise titanium stable isotope measurements by double-spike high resolution MC-ICP-MS. *J. Anal. At. Spectrom.* **29**, 1444-1458.

Millet, M.-A., Dauphas, N., Greber, N.D., Burton, K.W., Dale, C.W., Debret, B., Macpherson, C.G., Nowell, G.M. and Williams, H.M. (2016) Titanium stable isotope investigation of magmatic processes on the Earth and Moon. *Earth Planet. Sci. Lett.* **449**, 197-205.

Morad, S. and Adin Aldahan, A. (1986) Alteration of detrital Fe-Ti oxides in sedimentary rocks. *Geol. Soc. Am. Bull.* **97**, 567-578.

Moreno, T., Querol, X., Castillo, S., Alastuey, A., Cuevas, E., Herrmann, L., Mounkaila, M., Elvira, J. and Gibbons, W. (2006) Geochemical variations in aeolian mineral particles from the Sahara–Sahel Dust Corridor. *Chemosphere* **65**, 261-270.

Moreno, T., Pérez, N., Querol, X., Amato, F., Alastuey, A., Bhatia, R., Spiro, B., Hanvey, M. and Gibbons, W. (2010) Physicochemical variations in atmospheric aerosols recorded at sea onboard the Atlantic–Mediterranean 2008 Scholar Ship cruise (Part II): Natural versus anthropogenic influences revealed by PM10 trace element geochemistry. *Atmos. Environ.* **44**, 2563-2576.

Padoan, M., Garzanti, E., Harlavan, Y. and Villa, I.M. (2011) Tracing Nile sediment sources by Sr and Nd isotope signatures (Uganda, Ethiopia, Sudan). *Geochim. Cosmochim. Acta* **75**, 3627-3644.

Paine, M.D., Anand, R.R., Aspandiar, M., Fitzpatrick, R.R. and Verrall, M.R. (2005) Quantitative heavy-mineral analysis of a Pliocene beach placer deposit in southeastern Australia using the AutoGeoSEM. *J. Sediment. Res.* **75**, 742-759.

Patchett, P., White, W., Feldmann, H., Kielinczuk, S. and Hofmann, A. (1984) Hafnium/rare earth element fractionation in the sedimentary system and crustal recycling into the Earth's mantle. *Earth Planet. Sci. Lett.* **69**, 365-378.

Pik, R., Deniel, C., Coulon, C., Yirgu, G., Hofmann, C. and Ayalew, D. (1998) The northwestern Ethiopian Plateau flood basalts: classification and spatial distribution of magma types. *J. Volcanol. Geotherm. Res.* **81**, 91-111.

Pik, R., Deniel, C., Coulon, C., Yirgu, G. and Marty, B. (1999) Isotopic and trace element signatures of Ethiopian flood basalts: evidence for plume–lithosphere interactions. *Geochim. Cosmochim. Acta* **63**, 2263-2279.

Plank, T. and Langmuir, C.H. (1998) The chemical composition of subducting sediment and its consequences for the crust and mantle. *Chem. Geol.* **145**, 325-394.

Pomerancblum, M. (1966) The distribution of heavy minerals and their hydraulic equivalents in sediments of the Mediterranean continental shelf of Israel. *J. Sediment. Res.* **36**, 162-174.

Prytulak, J., Vervoort, J.D., Plank, T. and Yu, C. (2006) Astoria Fan sediments, DSDP site 174, Cascadia Basin: Hf–Nd–Pb constraints on provenance and outburst flooding. *Chem. Geol.* **233**, 276-292.

Pye, K. (1987) *Aeolian dust and dust deposits*. Elsevier.

Revel, M., Ducassou, E., Grousset, F., Bernasconi, S., Migeon, S., Revillon, S., Mascle, J., Murat, A., Zaragosi, S. and Bosch, D. (2010) 100,000 years of African monsoon variability recorded in sediments of the Nile margin. *Quat. Sci. Rev.* **29**, 1342-1362.

Rudge, J.F., Reynolds, B.C. and Bourdon, B. (2009) The double spike toolbox. *Chem. Geol.* **265**, 420-431.

Schneiderman, J.S. (1995) Detrital opaque oxides as provenance indicators in river Nile sediments. *J. Sediment. Res.* **65**, 668-674.

Tang, M., Chen, K. and Rudnick, R.L. (2016) Archean upper crust transition from mafic to felsic marks the onset of plate tectonics. *Science* **351**, 372-375.

Taylor, S.R. and McLennan, S.M. (1985) *The continental crust: its composition and evolution*. Blackwell Scientific Publishing, Oxford.

Tian, S., Inglis, E.C., Creech, J.B., Zhang, W., Wang, Z., Hu, Z., Liu, Y. and Moynier, F. (2020) The zirconium stable isotope compositions of 22 geological reference materials, 4 zircons and 3 standard solutions. *Chem. Geol.* **555**, 119791.

Tompkins, H.G., Zieman, L.J., Ibañez-Mejia, M. and Tissot, F.L. (2020) Zirconium stable isotope analysis of zircon by MC-ICP-MS: methods and application to evaluating intra-crystalline zonation in a zircon megacryst. *J. Anal. At. Spectrom.* **35**, 1167-1186.

Van de Flierdt, T., Goldstein, S.L., Hemming, S.R., Roy, M., Frank, M. and Halliday, A.N. (2007) Global neodymium–hafnium isotope systematics—revisited. *Earth Planet. Sci. Lett.* **259**, 432-441.

Venkatarathnam, K. and Ryan, W.B.F. (1971) Dispersal patterns of clay minerals in the sediments of the eastern Mediterranean Sea. *Mar. Geol.* **11**, 261-282.

Vervoort, J.D., Patchett, P.J., Blichert-Toft, J. and Albarède, F. (1999) Relationships between Lu–Hf and Sm–Nd isotopic systems in the global sedimentary system. *Earth Planet. Sci. Lett.* **168**, 79-99.

Vervoort, J.D., Plank, T. and Prytulak, J. (2011) The Hf–Nd isotopic composition of marine sediments. *Geochim. Cosmochim. Acta* **75**, 5903-5926.

Vlastélic, I., Carpentier, M. and Lewin, É. (2005) Miocene climate change recorded in the chemical and isotopic (Pb, Nd, Hf) signature of Southern Ocean sediments. *Geochem. Geophys. Geosyst.* **6**.

von Eynatten, H. and Dunkl, I. (2012) Assessing the sediment factory: the role of single grain analysis. *Earth-Science Reviews* **115**, 97-120.

Wang, W., Huang, S., Huang, F., Zhao, X. and Wu, Z. (2020) Equilibrium inter-mineral titanium isotope fractionation: Implication for high-temperature titanium isotope geochemistry. *Geochim. Cosmochim. Acta* **269**, 540-553.

Weldeab, S., Emeis, K.-C., Hemleben, C. and Siebel, W. (2002) Provenance of lithogenic surface sediments and pathways of riverine suspended matter in the Eastern Mediterranean Sea: evidence from ^{143}Nd/^{144}Nd and ^{87}Sr/^{86}Sr ratios. *Chem. Geol.* **186**, 139-149.

Zhang, J., Dauphas, N., Davis, A.M. and Pourmand, A. (2011) A new method for MC-ICPMS measurement of titanium isotopic composition: Identification of correlated isotope anomalies in meteorites. *J. Anal. At. Spectrom.* **26**, 2197-2205.

Zhang, W., Wang, Z., Moynier, F., Inglis, E., Tian, S., Li, M., Liu, Y. and Hu, Z. (2019) Determination of Zr isotopic ratios in zircons using laser-ablation multiple-collector inductively coupled-plasma mass-spectrometry. *J. Anal. At. Spectrom.* **34**, 1800-1809.

TABLES

Table 1. *Titanium and Zr isotope compositions of the EMS sediments. See supplementary Table S1 for the full Zr isotope composition data. Data for εNd, ΔεHf and Zr/Al$_2$O$_3$ are from Klaver et al. (2015).*

sample ID	site/core section	εNd	ΔεHf	Al$_2$O$_3$/TiO$_2$	Al$_2$O$_3$/Zr	δ$^{49/47}$Ti$_{OL-Ti}$ (‰)	2s	δ$^{94/90}$Zr$_{Zr\ NIST}$ (‰)	2s
AMS-001	125-3-4-110	-10.1	1.2	17.3	0.062	0.223	0.022	0.022	0.013
AMS-025	box core 33.13 °N 23.00 °E	-10.0	-3.2	16.2	0.025	0.186	0.022	0.006	0.016
AMS-032	125A-8-1-102-104	-10.2	7.6	21.4	0.120	0.218	0.022	0.041	0.016
AMS-034	374-2-2-70-72	-10.3	6.4	19.9	0.094	0.242	0.022	0.037	0.016
AMS-035	374-4-3-30-32	-10.3	7.7	21.0	0.105	0.235	0.022	0.019	0.016
AMS-036	374-6-3-110-112	-9.9	2.3	18.9	0.070	0.226	0.022	0.023	0.013
AMS-039	374-14-1-52-54	-10.3	7.2	21.1	0.140	0.210	0.022	0.027	0.013
AMS-002	125-7-2-30	-8.8	1.6	18.2	0.064	0.197	0.022	0.013	0.013
AMS-004	128-3-3-20	-8.2	-6.8	14.6	0.025	0.170	0.022	0.022	0.016
AMS-006	128-7-3-100	-8.8	6.3	19.9	0.086	0.209	0.022	0.020	0.013
AMS-007	128-11-1-100	-8.4	5.4	20.3	0.094	0.194	0.022	0.012	0.009
AMS-009	130-2-3-110	-8.2	2.6	16.9	0.057	0.209	0.022	0.032	0.013
AMS-029	box core 32.75 °N 29.00 °E	-8.0	-3.7	15.6	0.043	0.191	0.022	0.006	0.016
AMS-031	125A-6-1-51-53	-8.5	0.9	16.7	0.061	0.228	0.022	0.014	0.011
AMS-012	130-6-4-80	-6.3	4.9	16.0	0.066	0.200	0.022	0.021	0.009
AMS-028	box core 31.88 °N 29.41 °E	-6.4	-4.2	14.1	0.036	0.186	0.022	-0.006	0.009
AMS-046	378-8-2-101-103	-6.6	4.4	22.5	0.111	0.223	0.022	0.050	0.008
AMS-047	378A-1-3-127-129	-6.6	5.5	20.9	0.110	0.210	0.022	0.011	0.013
AMS-048	378A-3-6-103-105	-6.5	2.2	19.1	0.101	0.172	0.022	0.027	0.011
AMS-010	130-5-2-50	-2.0	5.0	10.9	0.064	0.164	0.022	0.009	0.009
AMS-011	130-6-1-120	-2.3	5.7	12.3	0.076	0.173	0.022	0.009	0.009
AMS-020	971B-4H-5-100	-2.8	3.3	14.3	0.064	0.170	0.022	0.013	0.009
AMS-022	971B-13X-1-55	-2.8	2.4	14.1	0.057	0.174	0.022	0.009	0.008
AMS-023	971B-19X-4-75	-2.4	0.3	13.5	0.040	0.181	0.022	0.019	0.009

Table 2. *Composition of the Saharan dust and Nile sediment components as compiled from literature data (see text for data sources and supplementary Dataset 1) and estimated from regression modelling of the EMS sediment samples.*

	εNd	**±**	**2se**	**Ti/Nd**	**±**	**2s**	**$\delta^{49/47}Ti_{OL\text{-}Ti}$**	**±**	**2se**	**Zr/Nd**	**±**	**2s**	**$\delta^{94/90}Zr_{Zr\ NIST}$**	**±**	**2se**
EMS sediments															
group 1	-10.18	±	0.15	136	±	24	0.226	±	0.009	4.80	±	1.57	0.028	±	0.007
group 2	-8.52	±	0.23	123	±	21	0.208	±	0.012	5.32	±	0.97	0.018	±	0.008
group 3	-6.48	±	0.12	131	±	22	0.201	±	0.022	4.49	±	1.04	0.027	±	0.017
group 4	-2.47	±	0.31	200	±	47	0.172	±	0.005	6.74	±	3.43	0.012	±	0.009
Sahara dust															
data	-13.82	±	0.80	106	±	71	n.d.			6.11	±	4.56	n.d.		
from regression	N/A			100	+	38	0.266	+	0.044	3.88	+	1.79	0.037	+	0.018
					-	47		-	0.024		-	2.10		-	0.011
Nile sediment															
data	2.56	±	1.15	738	±	333	n.d.			13.76	±	6.45	n.d.		
from regression	N/A			195	+	78	0.153	+	0.015	7.12	+	2.97	0.009	±	0.010
					-	64		-	0.020		-	2.51			